International Journal of Biological Macromolecules 340 (2026) 150022

Contents lists available at ScienceDirect

International Journal of Biological Macromolecules

journal homepage: www.elsevier.com/locate/ijbiomac

Neutralizing nanobodies against SARS-CoV-2 recognizing highly conserved epitopes at the Spike's S2 subunit

Daniel Polo-Megías [a,*], Mario Cano-Muñoz [a,1], Philipp Trolese [a,b], Sara Lestani [a,2], Ilaria La Rocchia [a,3], Andrea Pierangelini [b,4], Benedetta Fongaro [b], Patrizia Polverino de Laureto [b], Francisco J. Morales-Yánez [c,d], Jonathan Vaneyck [c,d], Alain Vanderplasschen [e], Thomas Decoville [f], Géraldine Laumond [f], M. Carmen Salinas-Garcia [a], Ana Cámara-Artigas [g], José A. Gavira [h], Christiane Moog [f,i], Mireille Dumoulin [c,d], Francisco Conejero-Lara [a,*]

[a] Departamento de Química Física, Instituto de Biotecnología y Unidad de Excelencia de Química Aplicada a Biomedicina y Medioambiente (UEQ), Facultad de Ciencias, Universidad de Granada, 18071, Granada, Spain
[b] Department of Pharmaceutical and Pharmacological Sciences, Via Marzolo 5, 30131, Padova, Italy
[c] Nano-Antibodies to Explore Protein Structure and Functions (NEPTUNS), Centre for Protein Engineering, InBios, Department of Life Sciences, University of Liège, Liège, Belgium
[d] AlpaNano, Centre for Protein Engineering, InBios, Department of Life Sciences, University of Liège, Liège, Belgium
[e] Immunology-Vaccinology, FARAH and Faculty of Veterinary Medicine, Department of Infectious and Parasitic Diseases, University of Liège, Liège, Belgium
[f] Laboratoire d'ImmunoRhumatologie Moléculaire, Institut National de la Santé et de la Recherche Médicale (INSERM) UMR_S 1109, Institut Thématique Interdisciplinaire (ITI) de Médecine de Précision de Strasbourg, Transplantex NG, Faculté de Médecine, Fédération Hospitalo-Universitaire OMICARE, Fédération de Médecine Translationnelle de Strasbourg (FMTS), Université de Strasbourg, F-67000, Strasbourg, France
[g] Department of Chemistry and Physics, University of Almería, Agrifood Campus of International Excellence (ceiA3), Research Center for Mediterranean Intensive Agrosystems and Agri-Food Biotechnology (CIAIMBITAL), Carretera de Sacramento s/n, Almería, 04120, Spain
[h] Laboratorio de Estudios Cristalográficos, IACT-CSIC, Armilla, 18100, Granada, Spain
[i] Vaccine Research Institute (VRI), F-94000 Créteil, France

ARTICLE INFO

Keywords:
X-ray crystallography
Isothermal titration calorimetry
Single-domain antibodies (sdAbs)

ABSTRACT

The formation of a six-helix bundle between the conserved heptad-repeat regions 1 and 2 (HR1 and HR2) in SARS-CoV-2 Spike's S2 subunit is essential for membrane fusion and represents a promising therapeutic target. Previously, we reported recombinant proteins named CoVS-HR1, which mimic the HR1 region and block its interaction with HR2, inhibiting viral fusion. Moreover, they are recognized by plasma antibodies from COVID-19 convalescent patients. In this work, we generated camelid heavy-chain-only antibody fragments (VHHs), also named nanobodies (NBs), against a CoVS-HR1 variant mimicking the full HR1 region. A first generation of selected NBs bound HR1 with high affinity and competed with HR2. Notably, this set of NBs exclusively recognized the C-terminal half of HR1, and two of them showed mild neutralizing activity in cell infection assays. Using a truncated CoVS-HR1 variant (N2C), we selected a second generation of NBs targeting specifically the N-terminal half of HR1. However, these NBs did not demonstrate neutralizing activity, possibly due to their low binding affinities. Several NB epitopes were delineated by hydrogen-deuterium exchange and mass spectrometry analysis, and the crystal structure of a ternary complex between an HR1-mimetic protein and two NBs was determined, confirming competition with HR2. Intriguingly, we found cooperative binding effects between NBs targeting each half of HR1, but these did not result in detectable inhibitory synergy. These findings demonstrate

* Corresponding authors.
E-mail addresses: danielpm@ugr.es (D. Polo-Megías), conejero@ugr.es (F. Conejero-Lara).
[1] Present address: Department of Biotechnology and Environmental Protection, Estación Experimental del Zaidín, Consejo Superior de Investigaciones Científicas, Granada, 18008, Spain
[2] Present address: Institute for Research in Biomedicine, Università della Svizzera italiana, 6500 Bellinzona, Switzerland
[3] Present address: Department of Biomedical Sciences, University of Padua, 35131 Padova, Italy.
[4] Present address: Target Discovery Institute, Center for Medicines Discovery, Nuffield Department of Medicine, University of Oxford, Oxford, United Kingdom

https://doi.org/10.1016/j.ijbiomac.2025.150022
Received 14 August 2025; Received in revised form 13 December 2025; Accepted 29 December 2025
Available online 6 January 2026

the existence of neutralizing epitopes in the S2 HR1 region and provide a foundation for future development of enhanced neutralizing NBs focused on specific epitopes using HR1-mimetic proteins.

1. Introduction

The COVID-19 pandemic, caused by severe acute respiratory syndrome coronavirus 2 (SARS-CoV-2), has been the most significant global health crisis in the past decade. Although rapid vaccine development and deployment have helped control the outbreak, long-term protection remains a challenge due to waning immunity from natural infection and vaccination, as well as the emergence of immune-evasive variants [1,2]. The virus's high mutation rate further complicates efforts to predict its evolution and control its spread [3]. Unlike vaccines, the development of effective therapeutics that provide immediate treatment for severe cases has progressed at a slower pace. Despite extensive research into both viral- and host-targeting strategies [4], no specific and universally approved antiviral treatment for SARS-CoV-2 exists. More than five years since the first reported cases, the ongoing battle against the virus underscores the urgent need for effective and safe antiviral agents.

Like other members of the genus *Coronavirus*, SARS-CoV-2 is an enveloped virus with a single-stranded, positive-sense RNA genome. Structurally, the virion consists of four main proteins: nucleocapsid (N), membrane (M), envelope (E), and spike (S) [5]. The S glycoprotein, which decorates the viral envelope, plays a crucial role in the initial steps of viral infection by specifically binding to the human angiotensin-

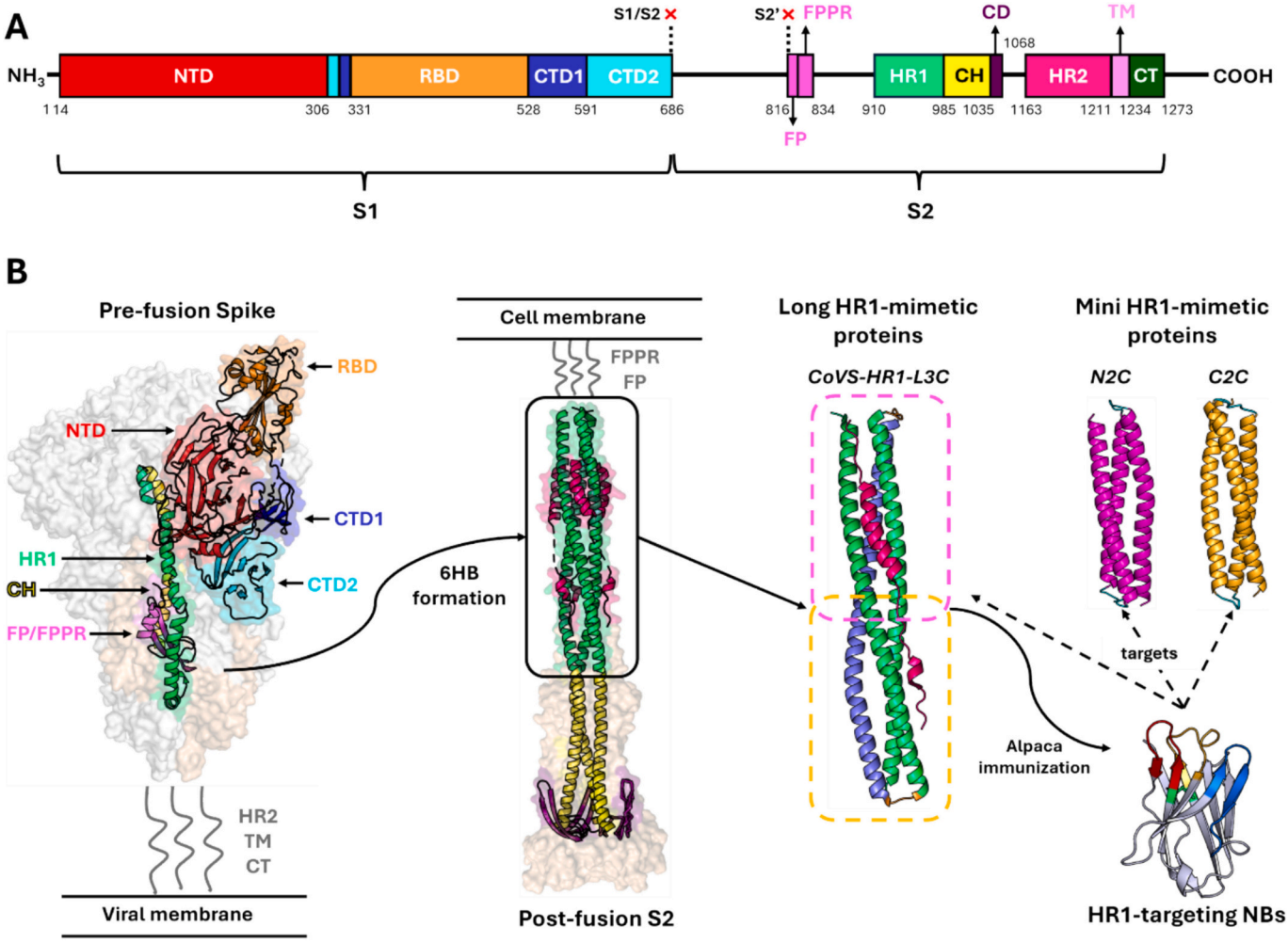

Fig. 1. Structure and domains of SARS-CoV-2 Spike and CoVS-HR1 proteins used for nanobody selection. A) Schematic representation of the different domains constituting the Spike protein of SARS-CoV-2. S1 subunit is formed by the N-terminal domain (NTD), receptor binding domain (RBD) and C-terminal domains 1 and 2 (CTD1 and CTD2). S2 consists of the fusion peptide (FP), fusion peptide proximal region (FPPR), heptad-repeat region 1 (HR1), central helix (CH), connector domain (CD), heptad-repeat region 2 (HR2), transmembrane domain (TM) and cytoplasmatic tail (CT). Cleavage sites S1/S2 (canonical furin-like: $PRRAR_{685}\downarrow$) and S2' ($KPSKR_{815}\downarrow$) have been included. B) Overview of the structural changes experienced by the S protein during the fusion process and inhibition strategy with HR1-mimetic proteins. The prefusion spike image shows a Cryo-EM structure (PDB ID: 6VSB) with one RBD in the "up" conformation (colored in orange). S1 and S2 subunits are represented as ribbons colored according to the domains depicted in A). The rest of S1 and S2 subunits have been rendered with a white translucent surface for the sake of clarity. Unsolved regions are indicated with gray lines. Postfusion conformation of the S2 subunits corresponds to another Cryo-EM structure (PDB ID: 6XRA). CoVS-HR1 image corresponds to the crystallographic structure of the complex between CoVS-HR1-L3B protein (blue and green ribbons) and the HR2-derived peptide V39E (carmine ribbon) (PDB ID: 7ZR2). The mini proteins images represent theoretical models of the two mini proteins mimicking the N-terminal half (N2C) and the C-terminal half (C2C) of HR1 (originally derived from L3C). The NB image is the predicted model of NB118 obtained from its sequence using Alphafold2 (server ColabFold). In this image the CDR1, CDR2, and CDR3 have been colored in blue, green, and red, respectively. The disulfide bond between the framework regions 1 and 3 (FR1 and FR3) has been highlighted in yellow. All the images have been rendered using PyMOL (Schrödinger LLC).

converting enzyme 2 (hACE2) receptor. This protein is synthesized as a homotrimer, with each monomer comprising two functionally distinct domains, S1 and S2 (Fig. 1A). The S1 domain includes the N-terminal domain (NTD), the receptor-binding domain (RBD), which is critical for receptor recognition and initial binding, and two C-terminal domains (CTDs). The S2 domain is divided into several key functional regions that mediate membrane fusion: fusion peptide (FP), heptad repeat region 1 (HR1), central helix (CH), connector domain (CD), heptad repeat region 2 (HR2), transmembrane domain (TM), and cytoplasmic tail (CT) [5,6]. For successful viral entry into the host cell, the S protein undergoes a series of proteolytic cleavages and conformational changes. The binding of the RBD to hACE2 exposes a cleavage site within S2, known as the S2' site, which is processed by the host transmembrane protease serine 2 (TMPRSS2) at the plasma membrane or by cathepsin L in the lysosome, depending on the entry pathway (cell surface or endosomal) [6]. Cleavage at the S2' site triggers irreversible conformational changes in S2, accompanied by S1 dissociation. During this process, FP inserts into the host cell membrane, while the S2 subunit is anchored to the viral membrane by the TM region. The S2 conformational change culminates in the formation of a highly stable trimeric six-helix bundle (6HB) structure, driven by antiparallel association between HR1 and HR2 (Fig. 1B). The energetically favorable structural reorganization drives the juxtaposition of the viral and cellular membranes, promoting their fusion and resulting in the formation of a fusion pore through which the virus releases its genetic material into the host cell [2,5–7].

The HR1 and HR2 regions are highly conserved across different coronaviruses [8], including novel SARS-CoV-2 variants of concern (VOCs) [9], making them attractive targets for the development of fusion inhibitors. In other enveloped viruses with class I fusion proteins, HR1/HR2-derived peptides have been extensively studied as potential inhibitors over the past few decades. In the early 1990s, it was discovered that peptides derived from the HR2 region of the gp41 subunit of human immunodeficiency virus type 1 (HIV-1) inhibit viral fusion [10]. This breakthrough paved the way for further research, leading to the development of HR2-derived peptides targeting viruses such as MERS-CoV [11], SARS-CoV [8], and SARS-CoV-2 [12,13]. HR1-derived peptides have also been explored as fusion inhibitors but exhibit much lower potency due to their tendency to oligomerize under physiological conditions in the absence of the HR2 counterpart [14]. However, the redesign of these peptides through different strategies to induce their trimerization in stable coiled coil structures significantly enhanced their inhibitory potential. This approach has proven effective in both HIV-1 [15–17] and SARS-CoV-2 [18,19], converting HR1 peptides into potent fusion inhibitors.

All this evidence supports the transient exposure of HR1 and HR2 regions during membrane fusion, making them accessible to antibody recognition. However, most neutralizing monoclonal antibodies (mAbs) generated in response to SARS-CoV-2 target the spike S1 subunit, mainly the RBD and, to a lesser extent, the NTD [20,21]. S1-targeting mAbs neutralize the virus through different mechanisms, by impeding ACE2 recognition, locking the RBD in a 'down' conformation, or causing S1 shedding prematurely [20]. Several of these mAbs have been commercialized and used in passive immunotherapy to effectively treat severe cases of COVID-19 throughout the pandemic [22]. However, their therapeutic use is limited due to the natural virus spreading and evolution, with the new VOCs acquiring the ability to evade antibody neutralization through new mutations affecting mainly RBD and NTD [3,23]. The S2 subunit contains highly conserved regions that also induce immune responses against the virus, and several neutralizing antibodies have been detected so far, mainly targeting the stem helix and FP regions [24,25]. Due to the high conservation of these regions, most of the isolated Abs exhibit a broad neutralizing capacity against different SARS-CoV-2 variants and even other coronaviruses [26]. However, immunogenic epitopes within the S2 subunit are much less described in the literature, particularly the highly conserved HR1 and HR2 regions, despite some studies suggesting their potential utility in vaccine development [27,28].

Although they have proven to be reliable assets in the fight against viral infections, mAbs therapy is not flawless. Due to their large size, mAbs do not efficiently cross the pulmonary barrier when used to treat lung infections; as a result, large amounts of the drug need to be administered intravenously. Furthermore, their production is very expensive and difficult to scale up to cover global needs, limiting their use in pandemic situations. One potential alternative to mAbs is the use of the variable domains of camelid heavy-chain-only antibodies, referred to as VHHs, Nanobodies® (NBs), single-domain antibodies (sdAbs), or nano-antibodies. NBs retain full antigen specificity and binding capacity despite their small size (*i.e.* 15 kDa on average). Along with their small size, NBs possess extended complementary determining regions (CDRs), especially the CDR3, and a convex-shaped paratope, which allow them to access epitopes unattainable by conventional antibodies, such as those formed at grooves or clefts on the antigen surface [29]. The small size of NBs is particularly valuable when developing fusion inhibitors against the highly glycosylated S protein, with many glycan residues shielding important epitopes [30]. NBs possess several other advantageous features, including enhanced tissue penetration, high thermal stability, excellent solubility, ease of production, and low human immunogenicity [31]. Moreover, they are amenable to further modification through protein engineering techniques to increase their affinity or create multivalent molecules [32]. All these combined features make NBs interesting tools in many research fields, highlighting their use in the diagnosis and treatment of several disorders such as cancer, autoimmune diseases, amyloid diseases, and viral infections [33,34]. Different studies have reported the potential use of NBs as fusion inhibitors of viruses like HIV-1, targeting both gp120 [35] (analogous to the S1 subunit) and gp41 [36] subunits. Since the emergence of SARS-CoV-2, several groups have worked on the development of neutralizing NBs against this virus [37,38]. However, similarly to what is observed with mAbs, most NBs target the S1 protein, whereas NBs against S2 have been much less studied. Nevertheless, potent *in vitro* and *in vivo* neutralization capacity has been reported for NBs targeting this subunit [39].

We have previously designed single-chain chimeric recombinant proteins that accurately mimic the HR1 coiled-coil helix trimer of gp41 in HIV-1. These proteins interact with HR2 peptides, effectively blocking the viral fusion process and inhibiting various HIV-1 strains *in vitro* [17,40–42]. Given the similarities between the fusion machinery of HIV-1 and SARS-CoV-2, we recently developed analogous chimeric coiled-coil proteins, named CoVS-HR1 (Fig. 1B), which mimic the HR1 region of the S2 subunit of SARS-CoV-2. These proteins also bind strongly to HR2 peptides and exhibit inhibitory activity against several viral strains *in vitro* [19,43,44]. Notably, we discovered that CoVS-HR1 proteins are recognized by antibodies present in the serum of convalescent SARS-CoV-2 patients at levels similar to those for the viral RBD [19], highlighting the immunogenic potential of the CoVS-HR1 proteins.

To further explore the antigenicity and neutralizing susceptibility of these epitopes, we describe here the generation of alpaca-derived NBs against the HR1-mimetic protein L3C, alongside their production and detailed biophysical characterization. We thoroughly examined the NB–HR1 interaction, as well as the NBs' capacity to compete with the binding of a synthetic HR2 peptide to HR1. Additionally, we used truncated versions of L3C—designated N2C and C2C—representing the N- and C-terminal halves of the protein, respectively (Fig. 1B), to pinpoint the location of the NB epitopes. The epitopes of the most interesting NBs were further confirmed using hydrogen-deuterium exchange coupled to mass spectrometry (HDX-MS) and structurally characterized by X-ray crystallography. Our findings indicate that the C-terminal region of HR1 is highly immunogenic, with all NBs selected from the initial immunization with L3C targeting this region. SARS-CoV-2 *in vitro* inhibition assays identified two NBs with mild neutralization activity. In contrast, NBs targeting the N-terminal half of HR1 showed

lower binding affinity and no detectable neutralizing activity. Interestingly, we observed cooperative binding effects between NBs targeting distinct epitopes along the HR1 crevice, suggesting potential utility in designing multimeric NB-based inhibitors.

2. Materials and methods

2.1. Alpaca immunization and selection of NBs

An alpaca (*Vicugna pacos*) was immunized with six subcutaneous injections at weekly intervals with 100 μL of lipopolysaccharide (LPS)-free L3C protein (1 mg/mL) in HEPES buffer (pH 7) mixed with 100 μL of TMP Gerbu adjuvant at the Faculty of Veterinary Medicine of Liège. An immune library of NB genes was created as previously described [45]. In short, five days after the last immunization, 80 mL of peripheral blood were collected from the jugular vein, and lymphocytes were isolated by density gradient centrifugation with Lymhoprep™ tubes (Nycomed, Switzerland). Then, total RNA was purified with the RNeasy Plus mini kit (Qiagen, Hilden, Germany). The freshly extracted RNA was used as template for cDNA synthesis with oligo dT primers (ThermoFisher, Waltham, Massachusetts, USA). The library was constructed according to standard protocols of cloning *via* PCR amplification with leader-specific primers CALL1 and CALL2 (https://doi.org/10.1128/AAC.45.10.2807-2812.2001). Two DNA fragments were amplified: fragments of approximately 600 bp representing the heavy chain-only antibody repertoire and fragments of 900 bp representing the heavy-chain of conventional antibody repertoire. The PCR products were separated by agarose electrophoresis, the 700 bp band was excised from the gel and purified using the Nucleospin Gel and PCR Clean-up (Macherey-Nagel, Düre, Germany). Then, a nested PCR with PMCF and AE6 primers was performed to specifically amplify the NB sequences. The resulting PCR products containing the full repertoire of NB genes were purified and cloned into the phagemid pMECS with the *PstI* and *NotI* restriction enzymes (10.1007/978-1-61779-974-7_8). The resulting library of phagemids was used to transform TG1 *Escherichia coli* (Lucigen, Middleton, Wisconsin, USA). Transformants were collected in LB media and counted in several dilutions to estimate the size of the library. Finally, a colony PCR on 39 randomly selected colonies with primers MP57 and GIII was carried out to evaluate the percentage of clones bearing a phagemid containing a VHH gene. The cell suspension containing the whole repertoire of transformants (designated as library Joe-2) was supplemented with 10 % glycerol (*w/v*), stored at −80 °C. NBs were selected using a phage display protocol that has been described in detail in Appendix S1.

2.2. Protein and peptides preparation

CoVS-HR1 (*i.e.*, L3B, L3C, C2C, and N2C) proteins were produced and purified following previously described protocols [19,44]. For NBs production and purification, a general protocol with some variations was used [45]. A more detailed protocol can be found in Appendix S2. To sum up, the sequences of the NBs were cloned into pMECS or pHEN6 vectors and expressed in *E. coli* BL21(DE3) cells. Glycerol stocks from single colonies were used to inoculate LB medium, followed by scale-up in Terrific Broth supplemented with 100 μg/mL ampicillin, 1 mM magnesium chloride, and 0.1 (w/v) glucose. Protein expression was induced overnight with 1 mM IPTG at 27 °C. Cells were then harvested, lysed by sonication, and the soluble fraction was purified using nickel-tag affinity and ion exchange chromatography. Purity and identity were verified by SDS-PAGE and mass spectrometry. Purified NBs were stored at −80 °C in 50 mM sodium phosphate buffer (pH 7.4). For biophysical characterization, NB and CoVS-HR1 solutions were extensively dialyzed against the appropriate buffer, centrifuged (30 min, 14,000 rpm, 4 °C), and their concentrations measured by UV absorption at 280 nm using extinction coefficients obtained *via* ExPasy ProtParam (https://web.expasy.org/protparam/). Unless otherwise noted, experiments were conducted in 50 mM sodium phosphate buffer, pH 7.4. The synthetic HR2 peptide V39E (S protein residues 1164–1202) was obtained from Genecust (Boynes, France) with >95 % purity, in *N*-acetylated and C-amidated form, and including a C-terminal SGGY tag to enable UV-based quantification at 280 nm. Peptide stocks were freshly prepared by dissolving lyophilized peptide in buffer followed by pH readjustment. The solution was then centrifuged (30 min, 14,000 rpm, 4 °C) to remove undissolved material, and concentration was determined spectrophotometrically in a Varian Cary 50 spectrophotometer (Varian, California, USA; now Agilent Technologies). Protein-peptide mixtures were prepared at defined molar ratios based on concentrations calculated from UV absorbance at 280 nm.

2.3. Secondary structure analysis of the NBs using circular dichroism (CD)

CD spectra of the NBs were collected using a Jasco J-715 spectropolarimeter (Jasco Corporation, Tokyo, Japan) equipped with a Peltier temperature control unit. Far-UV measurements were carried out at 25 °C, covering a range of 260–200 nm, at a 50 nm/min scan rate, 1 nm step resolution, 2 s response time, and 1 nm bandwidth. The resulting spectrum was an average of 10 scans. Upon baseline subtraction, the spectrum was finally normalized to molar ellipticity ([θ], in deg.·cm^2·dmol^{-1}) or mean-residue ellipticity (MRE, in deg.·cm^2·dmol^{-1}·res^{-1}) and the percentage of secondary structure was estimated using the K2D3 online software [46]. All measurements were carried out at 25 °C using a 1 mm quartz cuvette and a sample concentration of 25 μM.

2.4. Hydrodynamic radius estimation of the NBs using dynamic light scattering (DLS)

DLS measurements were carried out on a Malvern μV instrument (Malvern Panalytical Ltd., Malvern, UK) at 25 °C in sets of 30 independent acquisitions with 10 s acquisition time. The collected data were processed using the instrument's software to obtain the hydrodynamic radius (R_h) distributions of each NB sample. Experiments were performed using a 1.5 mm DLS quartz cuvette and a sample concentration of 25 μM. Before each measurement, samples were extensively centrifuged for 30 min at 14,000 rpm (4 °C) in a bench centrifuge.

2.5. Characterization of the thermal stability of the NBs and their interaction with HR1 using differential scanning calorimetry (DSC)

DSC thermograms were collected using a PeakQ-DSC or a VP-DSC microcalorimeter from MicroCal LLC, equipped with an autosampler (Malvern Panalytical, Malvern, UK). The scans were usually the result of runs from 10 °C to 120 °C, with a scan rate of 90 °C/h and a sample concentration of 25 μM. Two baseline scans were recorded before each sample scan by filling both the sample and reference cell of the instrument with buffer. The excess heat capacity (ΔC_p) relative to the buffer was calculated from the experimental DSC thermograms using Origin software (OriginLab, Northampton, MA) and normalized per mole of NB. For NBs biophysical characterization, unfolding enthalpy (ΔH_m) and melting temperature (T_m) were calculated by fitting experimental thermograms with a two-state reversible model (*Native* $(N) \rightleftharpoons$ *Unfolded* (U)). To compare the T_m differences between the L3C–NB and L3C–NB–V39E mixtures with the NB alone, the melting temperature was taken as the temperature at the maximum of the heat capacity peak corresponding to the NB unfolding transition.

2.6. Characterization of the interaction of the NBs with HR1 using isothermal titration calorimetry (ITC)

ITC thermograms were obtained using a Microcal VP-ITC calorimeter (Malvern Panalytical, Malvern, UK). For the 1st-gen NBs, L3C protein

was titrated at 25 °C with 25–30 injections of 10 μL NB solution with 480 s intervals. Thus, L3C concentration in the cell was 10 μM, and the concentration of the NBs in the syringe was around 150 μM. For 2nd-gen NBs, the reverse titration and a temperature of 37 °C were chosen due to the low binding affinity and production yield of these NBs. The thermograms were baseline corrected, and the peaks were integrated to determine the heat produced by each ligand injection using the software of the instrument (Origin software). Residual heats due to unspecific binding or ligand dilution were estimated from the area of the final peaks of the titrations when the protein is saturated with ligand. Each heat was normalized per mole of injected ligand. The resulting binding isotherms were fitted using a binding model of n independent and equivalent sites implemented in Origin software, allowing the determination of the apparent binding (K_b) and dissociation (K_d) equilibrium constants, binding enthalpy (ΔH), binding entropy (ΔS), Gibbs energy (ΔG) and binding stoichiometry (n). Error estimations for each magnitude were obtained from each individual isotherm fit using a 95 % confidence interval of the fitting parameters, provided by Origin's nonlinear fitting tool. For the cooperative binding studies with ternary complexes, L3C protein was mixed with one of the NBs at a molar ratio of 1:1.5 or 1:2 and incubated for at least 15 min at room temperature. This mixture was titrated with the second NB at the concentrations described above.

2.7. Evaluation of the ability of the NBs to compete with HR2 using size exclusion chromatography (SEC)

To further evaluate competition of NBs with HR2, SEC experiments were conducted using a Superdex 75 10/300 GL column connected to an ÄKTAprime plus FPLC system (GE Healthcare Bio-Sciences AB, Sweden). Consecutive chromatograms were collected by injecting 100 μL of each sample and eluting at 1 mL/min flow rate at room temperature. The concentration of samples ranged between 0.5 and 1 mg/mL. The elution buffer consisted of 50 mM sodium phosphate (pH 7.4) containing 150 mM NaCl. The final chromatograms were detected by UV absorption at 280 nm and normalized per mole of injected NB for comparative purposes.

2.8. Delineation of the binding epitopes of the NBs using hydrogen/deuterium exchange (HDX) coupled to mass spectrometry (MS)

HDX-MS samples were prepared by mixing the protein L3B with the NBs in a molar ratio of 1:2. The mixture was then incubated at room temperature for 15 min before proceeding with the H/D reaction. After that time, an aliquot (1 μL) of each sample was diluted 10-fold in deuterated buffer (20 mM sodium phosphate (pH 7.4) containing 100 mM NaCl and prepared in 99.9 % D_2O) and was allowed to exchange for 1 min at room temperature. Reaction was quenched by the addition of the quenching buffer (7 M Gnd-HCl, 0.8 % formic acid, adjusted to pH 2.21) to reach a four-fold dilution. To aid protein denaturation, the samples were left to quench for 4 min before the final dilution with 0.8 % formic acid to reach a final Gnd concentration below 2 M. Finally, digestion was achieved using an in-line pepsin column (Enzymate™ BEH Pepsin Column, Waters), thermostated at 15 °C and eluted at a constant flow rate (40 μL/min) with 0.23 % (*v*/v) aqueous formic acid. Digestion products were online trapped on an Acquity UPLC BEH C18 VanGuard Pre-column (Waters) and eluted on an Acquity UPLC BEH C18 column (Waters) using a linear acetonitrile gradient from 3 % to 35 % in 11 min, at a constant flow rate of 40 μL/min and with 0.1 % formic acid. The effluent was analyzed using a Xevo G2-S Q-TOF mass spectrometer (*m/z* 50–2000) operated in MSE mode, with argon employed as the collision gas. Pepsin digestion peptic fragments were identified using the Protein Lynx Global Server 3.0 and then analyzed with DynamX 3.0 software (Waters). For the analysis, only the fragments meeting the following criteria were included: i) 5 %-retention time window in the chromatographic separation; ii) maximum MH+ error of 6 ppm; iii) at least 2 ion products identified for each peptic fragment; iv) a minimum of 0.3 ion products generated per amino acid in the fragment; v) fragments containing more than 33 amino acids were excluded, due to identification ambiguity and poor sequence localization. Triplicates were made for each sample. HDX-MS measurements were performed using a Xevo G2S Q-TOF (Waters) mass spectrometer equipped with a standard electrospray ionization source, an Acquity M-class UPLC (Waters), an Automation 2.0 sample workstation (Waters), and an HDX PAL autosampler (Leap Technologies, Carrboro, NC, USA). Leu-enkephalin (Waters) was continuously infused as the reference lock mass.

HDX data were analyzed using Waters DynamX software and mapped onto the crystal structure of the L3B–V39E complex (PDB ID: 7ZR2). Average exchange values from the identified peptides were assigned to the B-factor field of each residue and visualized in PyMOL with a custom script using a blue (deprotection) – white (no change) – magenta (protection) colour gradient.

2.9. Evaluation of the neutralizing capacity of the NBs in virus neutralization assays

One day prior infection, Vero 76 cells were plated on a 96-well plate at 12,500 cells/well. 50 μL of serial 4-fold dilutions of NBs (2-fold concentrated) and 50 μL WT SARS-CoV-2 viruses (B1 D614G genotype or Alpha B.1.1.7 (UK isolate) at Multiplicities Of Infection (MOI) of 80 were incubated for 1 h. For combination analysis, 25 μL of serial 2-fold dilutions of NB118 and NB184 (fourfold concentrated) were mixed NBs with the two SARS-CoV-2 viruses tested. Virus NB mixtures were cultured with the Vero cells for 2 days. After the 2 days, cells were fixed with methanol for 20 min, washed with PBS, and stained with anti-nucleocapsid Ab (GTX135357, Genetex, Hsinchu City, Taiwan) at 1/200 dilution in permwash (B&D) for 45 min at room temperature. Nucleocapsid-positive cells were revealed with a donkey anti-Rabbit monoclonal Ab (Alexa 647; A31573, Invitrogen, Thermo Fisher Scientific, Waltham MA) diluted at 1/200 in PBS 5 % FCS for 45 min at room temperature. In parallel, total living cells were detected by Sytox green (S7020, Invitrogen) staining. Total cells (Sytox Green positive) and infected cells (nucleocapsid-positive) were counted using SpectraMax MiniMax Imaging Cytometer (Molecular Devices LLC, San Jose, CA). The percentage of infected cells in each well was calculated from the number of infected cells relative to the total number of living cells and then normalized by the percentage of infected cells in the controls in absence of inhibitor. Thereafter, the percentage of inhibition was calculated from the reduction in the percentage of infected cells in wells treated with inhibitor relative to the percentage of infected cells in control wells not treated with inhibitor using the formula:

$$\%\text{Inhibition} = 100 \bullet \frac{100 - \%\text{infected cells (treated)}}{\%\text{infected cells (control untreated)}}$$

The 50 % inhibitory concentration (IC_{50}) was defined as the protein concentration leading to a 50 % reduction in the percentage of infected cells.

2.10. Structure determination of the NBs–HR1 complexes using X-ray crystallography

For L3B–NB278–NB184 ternary complex crystallization, NBs were dialyzed against 10 mM Tris buffer (pH 7.5) and concentrated to ~500 μM (~6.5 mg/mL for NB278 and ~ 8 mg/mL for NB184). A mixture of both NBs was prepared, so the final concentration was ~250 μM. This mixture was then used to resuspend a previously lyophilized L3B protein prepared to reach a final concentration of ~250 μM, meeting a 1:1:1 mole ratio. Suitable crystallization conditions were first identified by the sitting-drop vapor diffusion method using commercially available screening kits: Structure Eco Screen and ProPlex (Molecular Dimensions,

Suffolk, UK). Droplets consisting of 1 μL complex solution and 1 μL reservoir solution were equilibrated at 15 °C against 200 μL reservoir solution in 48-well MRC Maxi Optimization plates (Cambridge, UK). Favorable conditions were then optimized to obtain improved crystals, with the best diffraction results obtained from the following condition: 0.15 M NaCl, 0.1 M Tris (pH 7.5), PEG 6000 50 % (*v*/v). Crystals were soaked with cryoprotectant (15 % glycerol) and flash-cooled in liquid nitrogen before data collection.

Data sets were collected at 100 K on the beamline XALOC at ALBA synchrotron (Barcelona, Spain) [47]. Diffraction data were indexed and integrated with the AutoPROC toolbox [48]. Data scaling was performed using the program Aimless from the CCP4 suite [49]. Data collection statistics are collected in Table S1. Molecular-replacement phasing using PHASER [50] was performed with the coordinates of the crystallographic structure of the chimeric protein mimic of SARS-CoV-2 Spike HR1 domain (PDB ID 7ZR2 [19]) and the nanobody coordinates available in the PDB with highest homology to the nanobodies NB278 and NB184 (PDB entries 5G5R [51] and 5LHR [52]). Refinement of the structures was performed using phenix.refine in the PHENIX suite [53]. TLS refinement was applied during the final stages of refinement, with 10 TLS groups identified by phenix.find_tls_groups. Manual model-building cycles were performed using COOT [54,55]. The quality of the structure was checked using MOLPROBITY [56] and PROCHECK [57]. Structural refinement statistics are collected in Table S1. The coordinates were deposited at the Protein Data Bank under the accession code 9RN6.

2.11. In silico structural analysis of the NBs–HR1 ternary complex

A computer analysis was performed on the ternary complex structure composed of the L3B protein and two nanobodies, NB278 and NB184, using YASARA Structure (v22.9.24; YASARA Biosciences), with default parameters unless otherwise specified. The structural model (PDB ID: 9RN6) was used without modifications for all calculations.

To quantify residue–residue contacts across the interfaces between L3B and each nanobody, we used the ListConRes command in YASARA, which calculates the number of atomic pairs between two residues that lie within a user-defined distance threshold. The parameters used were: Cutoff = 4.0 Å, this threshold defines the maximum distance for a contact to be considered; Subtract = VdWRadii, the Van der Waals radii of the atoms involved were subtracted from their interatomic distance, ensuring that only meaningful, non-clashing contacts were retained; Exclude = 4, covalently bonded atoms up to the fourth neighbor (1–4 interactions) were excluded from the analysis to avoid counting intramolecular contacts; Occluded = Yes, contacts that are geometrically blocked by intervening atoms (*i.e.*, not directly accessible) were excluded from the count. This approach enabled the estimation of interaction strength based on the number of atomic contacts between the residues of the nanobody and L3B. For each nanobody–L3B interface, contact counts were computed bidirectionally (L3B → NB and NB → L3B), acknowledging the asymmetry that can occur due to differences in surface exposure and geometry.

To calculate contact surface areas between L3B and each nanobody the ConSurf command in YASARA was used. We used a Cutoff and Subtract parameters of 1.4 Å and Van der Waals radii of the atoms involved respectively to account for the molecular surfaces between interacting chains while excluding the potential contribution of water molecules, thus capturing only tight intermolecular contacts. The percentage of hydrophobic surface was calculated based on the contact surface area of hydrophobic atoms (*i.e.*, carbons and their bound hydrogens) as recommended in the manual.

Molecular graphics and surface representations were generated in YASARA Structure for rapid assessment. Final renderings were performed using UCSF Chimera, with electrostatic surface potentials calculated using the AMBER force field and APBS solver, as described elsewhere [58]. Fig. 7A and B were created superposing the crystal structures of V39E peptide bound to L3B (PDB ID: 7ZR2) with the structure of NB278 and NB184 bound to L3B (PDB ID: 9RN6) using the Matchmaker algorithm implemented in ChimeraX (v1.9) [59].

3. Results

3.1. Selection of the first generation of NBs

One alpaca was immunized with L3C, and a specific NB library was constructed from the cDNA encoding NBs isolated from lymphocytes. The total size of the library was 8.4×10^9 transformants and 90 % of them had an insert of the expected size of a NB gene. Following three rounds of selection by phage display using L3C as target, eight different VHH's belonging to six different families were selected (Table S2): NB107, NB113, NB117, NB118, NB127, NB248, NB268, and NB278. NB107 and NB248 belong to the same family but differ by a single position in the CDR2 and CDR3 regions. NB268 and NB117 share the same CDR3 sequence but differ in their FR1, CDR1, and FR2 regions. NB107 differs in one residue at CDR3 and at CDR1 and CDR2 regions compared to NB 268 and NB 117. The remaining four families were each represented by one single NB. These NBs are referred to as the first generation of NBs (1st-gen NBs). The two NBs from family VI (*i.e.*, NB107 and NB248) contain an additional disulfide bridge between the CDR3 and FR2.

3.2. Purification and biophysical characterization of the 1st-gen NBs

All NBs were produced and purified in relatively high yields (1–20 mg/L of culture, depending on the NB) and with >95 % purity. Using CD spectroscopy and DLS, the secondary structure and oligomerization state of the eight NBs were analyzed at 25 °C in 50 mM sodium phosphate buffer (pH 7.4). All NBs were highly soluble in this buffer, showing far-UV CD spectra consisting with proteins rich in β-sheet structure (43–45 %) and hydrodynamic radius distributions corresponding to the monomeric form (1.5–1.9 nm) (Fig. S1). Formation of the disulfide bridge connecting the CDR1 and CDR3 loops was confirmed using Ellman's reagent (Fig. S2, Appendix S3). The thermal stability of the NBs was analyzed using DSC, yielding to thermograms with single endothermic transitions, melting temperatures (T_m) between 58 and 77 °C and an average unfolding enthalpy (ΔH_m) of 420 kJ/mol (Fig. S3). Biophysical data for each NB are listed in Table S3.

3.3. Study of the interaction of the 1st-gen NBs with HR1: competition with HR2 assessment and regional epitope mapping

Binding between each NB and the HR1-mimetic L3C was first assessed using DSC. Given that L3C unfolds at a very high temperature (T_m = 104 °C), the binding of NBs to L3C is expected to result in their thermal stabilization, observable by a positive thermal shift (ΔT_m) of the NB unfolding transition. This provided us with a quick and straightforward test to identify the tightest binding NBs, as higher binding affinities should correlate with higher thermal shifts and increased unfolding enthalpy increments. As expected, in the presence of L3C all NBs clearly exhibited a thermal stabilization, indicating that they all bind to L3C (Fig. 2A and Fig. S3). From this initial analysis, NB113 and NB118 emerged as the most promising candidates presenting the largest thermal shifts (ΔT_m = 11.5 °C and 10.7 °C, respectively), followed by NB278 and NB248 (ΔT_m = 7.5 °C and 7.3 °C, respectively) (Fig. 2B).

As described in previous works, CoVS-HR1 proteins are composed of three HR1 helices, two arranged in a parallel orientation, and the third one inverted in sequence and orientated in a reverse orientation with respect to the other two. Mutations were introduced in the two grooves between the parallel and reverse HR1 helices to establish appropriate stabilizing interactions. The amino acids forming the groove between the two parallel HR1 helices were not modified to faithfully mimic the viral HR1 groove, preserving the binding capacity to HR2 [19,43]. This

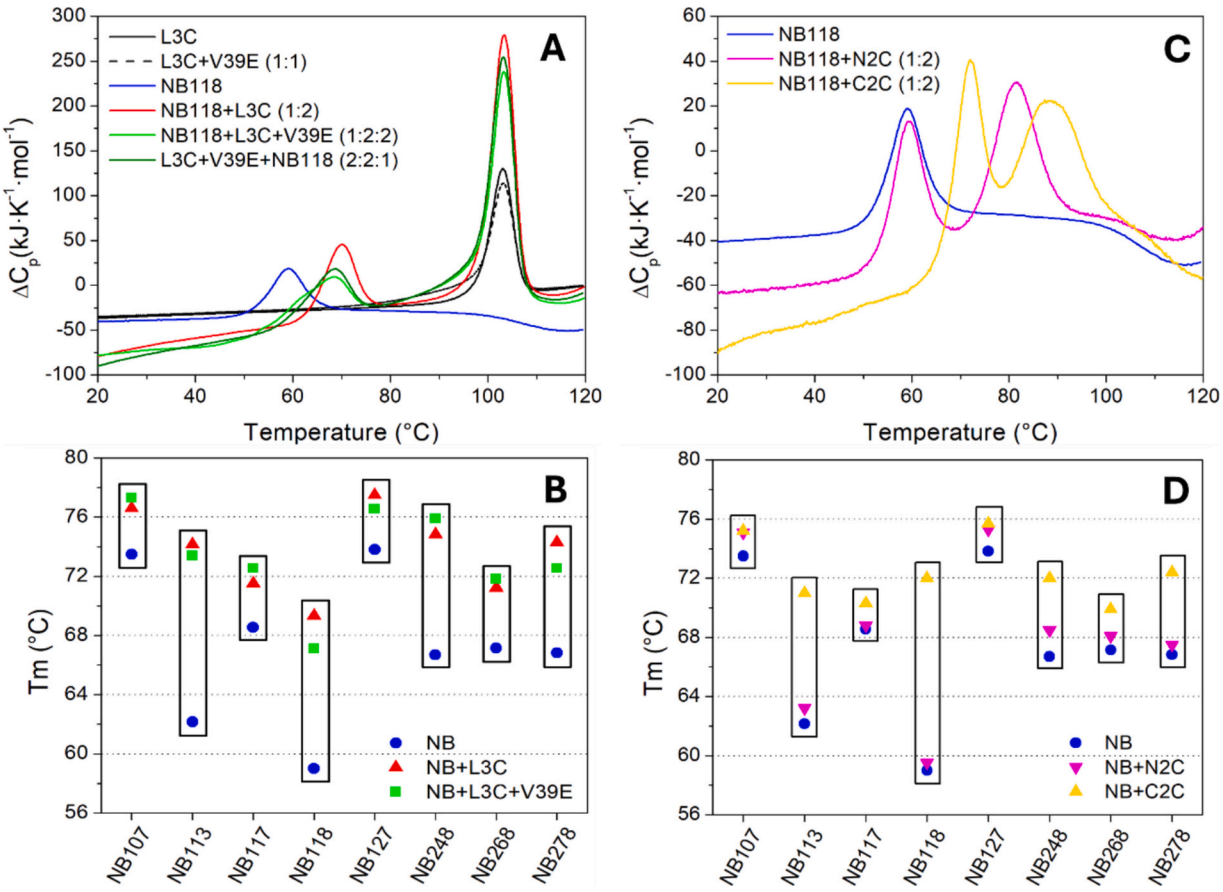

Fig. 2. DSC analysis of the interaction of 1st-gen NBs with HR1. A) DSC thermograms showing the thermal unfolding of NB118 in the presence of L3C and the V39E peptide at a molar ratio NB:L3C:V39E (1:2:2). Binding of NB118 to L3C results in its stabilization, evidenced by a sharper unfolding transition and in an increased T_m of the NB. When the V39E peptide is added, the stabilizing effect is partially reversed due to competition with the peptide for HR1 binding. B) Plot representing the different T_m values corresponding to each NB alone, bound to L3C, and in the competition experiment with V39E peptide. Competition is clear for NB118 and NB278 and to a lesser extent for NB113 and NB127. C) Thermal unfolding of NB118 in the presence of N2C and C2C mini proteins measured by DSC. Similarly, binding of the NB to the half-HR1 mimics N2C or C2C induces its stabilization, increasing the T_m of the NB. D) Plot representing the different T_m values corresponding to each NB alone and in the presence of C2C or N2C.

implies that only those NBs whose epitopes are located on the HR1 parallel crevice would be able to compete with viral HR2 and block 6HB formation. To further identify the candidates fulfilling this requirement, competition experiments were carried out with the HR2-derived peptide V39L. This peptide spans residues V_{1164}–E_{1202} (according to Spike S2 sequence numbering) and covers most of the HR2 length (Table S4). We have extensively used the V39E peptide in previous studies to analyze its interaction with the CoVS-HR1 proteins, and a crystallographic structure of the complex has been published (PDB ID: 7ZR2) [19,43,44].

In this way, ternary mixtures were prepared using the three components (NB, L3C, and V39E peptide) in two separate ways: (i) NB and L3C were mixed, and after 20 min of incubation at room temperature, the V39E peptide was added; (ii) L3C and V39E were mixed, and 20 min later the NB was added. In both cases, the molar ratio was kept constant at 1:2:2 (NB:L3C:V39E). Notably, when comparing mixtures (i) and (ii) prepared in different orders, thermograms were identical for all NBs. As observed in the DSC thermograms, the unfolding transition of those NBs competing with HR2 exhibited a negative shift in T_m compared to the transition observed in the absence of V39E. In contrast, those NBs with epitopes not overlapping the HR2 binding crevice showed unfolding transitions with T_m values that were either barely changed or slightly increased compared to the transition in the absence of V39E (Fig. 2A, B, and S3). Competition with HR2 was clearly found for NB118 and NB278, which exhibited a considerable decrease in T_m in the presence of the V39E peptide. NB113 and NB127 showed only a slight decrease in T_m, which was insufficient to draw a definitive conclusion about competitive binding. Conversely, NB107, NB117, NB248, and NB268 showed a further increased T_m when the peptide was added to the mix, indicating stabilization trough formation of a possible NB–L3C–V39E ternary complex. Additionally, SEC analysis was performed to assess both NB binding to L3C and competition with HR2 (Fig. S4). In these experiments, the intensity of the elution peak of the NB–L3C complex (≈ 11 min), in the presence and absence of the V39E peptide, was compared to that of the free NB (≈ 15 min). This analysis confirmed competition for NB113, NB127, NB118, and NB278, whereas the formation of ternary L3C–NB–V39E complexes was confirmed for the other NBs.

To better characterize the location of the epitopes of the 1st-gen NBs on the L3C molecule, DSC experiments using the N2C and C2C mini proteins were performed to analyze the stabilizing effect due to their binding to each NB (Fig. S5). These proteins also have relatively high thermal stability ($T_{m,\ N2C}$ = 81 °C, $T_{m,\ C2C}$ = 88.5 °C), so the binding of the NB to any of the proteins will also result in its thermal stabilization, whereas the absence of binding will leave the NB unfolding peak unchanged (Fig. 2C). Notably, six out of eight NBs appeared to bind only to C2C, mimicking the C-terminal half of HR1. NB107, NB127 exhibited small but clear positive T_m shifts in complex with C2C. However, in the presence of N2C a T_m shift could not be clearly determined due to overlapping between the NB and N2C unfolding peaks. Furthermore, the T_m shifts observed in these experiments were generally smaller than those seen in L3C binding studies, reflecting a weaker interaction of the

NBs with the mini proteins compared to L3C (Fig. 2D).

3.4. Study of the interaction of the 1st-gen NBs with HR1: thermodynamic binding parameters determination

More comprehensive thermodynamic data of the NB–HR1 interaction were obtained through ITC experiments where L3C was titrated with each NB at 25 °C (Fig. 3A, Fig. S6). The resulting isotherms exhibited sigmoidal shapes and indicated binding stoichiometries close to 1 (except for NB117 and NB127). The apparent dissociation constants (K_d) ranged from 10 to 500 nM and all NBs displayed negative binding enthalpies (ΔH) (Fig. 3B, Table S5). NB113, NB118, and NB278 stood out again due to their lower K_d values (9 nM, 30 nM, and 12 nM, respectively). Interestingly, NBs with higher K_d such as NB117, NB127, NB248, and NB268, showed higher binding enthalpies together with increased negative entropy contributions (ΔS) associated with the formation of the NB–L3C complex. Conversely, NBs with lower K_d, including NB107, NB113, NB118, and NB278, exhibited lower binding enthalpies and reduced binding entropy losses. In two instances (NB113 and NB118), the entropy contributions were even positive.

It is worth mentioning that by comparing DSC and ITC data it was confirmed that NBs with greater ΔT_m tend to have a lower K_d at 25 °C, although a strict relationship cannot be established either. This is likely due to the involvement of other factors such as the intrinsic stability of the NBs and the different binding enthalpies and heat capacities, which affect the changes in interaction strength with temperature.

3.5. Second generation of NBs: NBs targeting the HR1 N-terminal region

The core interaction between the N-terminal region of HR1 (residues V_{915}–K_{947}) and its counterpart in HR2 (residues I_{1179}–E_{1202}) has been described to play a critical role during SARS-CoV-2 entry [43,44,60], making it a particularly attractive target in the search for fusion inhibitors. A similar mechanism has been reported in HIV-1 [61]. To select NBs recognizing epitopes within this region, a new three-round panning campaign was carried out using the immune library Joe-2 and the N2C protein as target. Six new NBs belonging to three different families were selected, constituting the second generation of NBs (2nd-gen NBs; Table S2). One representative of each family (named NB147, NB184, and NB235) was successfully produced, purified, and characterized as described above. As expected, the new NBs exhibited similar biophysical properties to the 1st-gen NBs in terms of folding, oligomerization state, and thermal stability (Fig. S7, S8, and Table S3).

The interaction between the 2nd-gen NBs and HR1 was evaluated by DSC with the L3C protein. Smaller thermal shifts in the NB unfolding transition (ΔT_m between 0.8 and 2.3 °C) were observed compared to those of the 1st-gen NBs, suggesting that the 2nd-gen NBs exhibit reduced binding affinity. When the V39E peptide was added to the NB–L3C mixtures, clear competition was observed for NB184. However, the competitive effects for the other two NBs were less evident due to their small thermal shifts (Fig. 4A, C, and S8). SEC experiments were not as conclusive as those performed with the 1st-gen NBs because of the low affinity of the new NBs for L3C, although they confirmed HR2 competition with NB184 (Fig. S9), whereas the SEC chromatograms suggested the formation of ternary complexes for the other two NBs. It is expected that NB147 and NB235 would behave very similarly, as they share nearly identical CDR3 domains except for one residue (Table S2). Additionally, DSC analysis confirmed binding to the N2C protein, with NB147 potentially interacting with both N2C and C2C proteins (Fig. 4B, C, and S8).

To further investigate the thermodynamics underlying the interaction between L3C and each 2nd-gen NB, ITC experiments were conducted at 25 °C. Since ITC thermograms showed minimal binding heats at this temperature for NB147 and NB235, additional experiments were performed at 37 °C (Fig. S10). Reverse titration was employed due to the limited production yields of NB147 and NB235, with NBs at 10 μM in the instrument cell and L3C at approximately 150 μM in the syringe. Despite these adjustments, the resulting isotherms displayed a parabolic shape for NB147 and NB235, while NB184 had a more sigmodal titration curve (Fig. 4D), reflecting the higher binding affinity of this NB in respect of

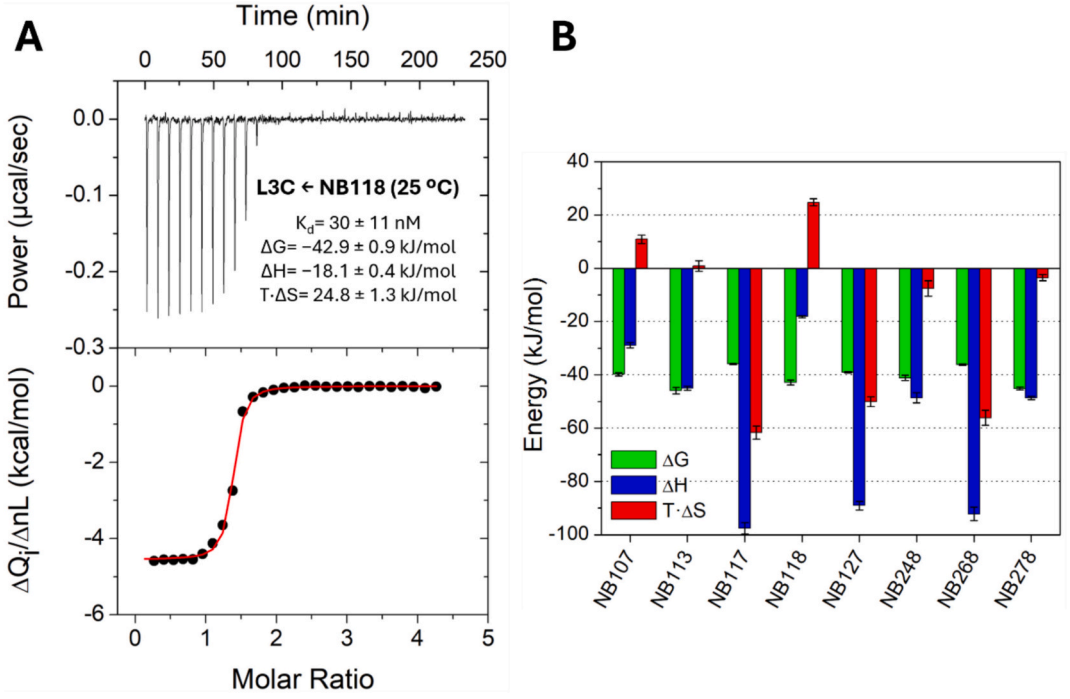

Fig. 3. ITC study of the interaction of 1st-gen NBs with HR1. A) ITC titration of L3C with NB118 measured at 25 °C. The upper panel represents the experimental thermogram corrected from baseline with negative heats of binding. The red line corresponds to the best fit using a model of n identical and independent sites. B) Binding thermodynamic parameters of the 1st-gen NBs calculated from the ITC data comparing binding ΔG, ΔH, and T·ΔS terms. Error bars were calculated from 95 % confidence intervals of the parameters estimated by the individual fits of the binding isotherm using a model of *n* independent sites.

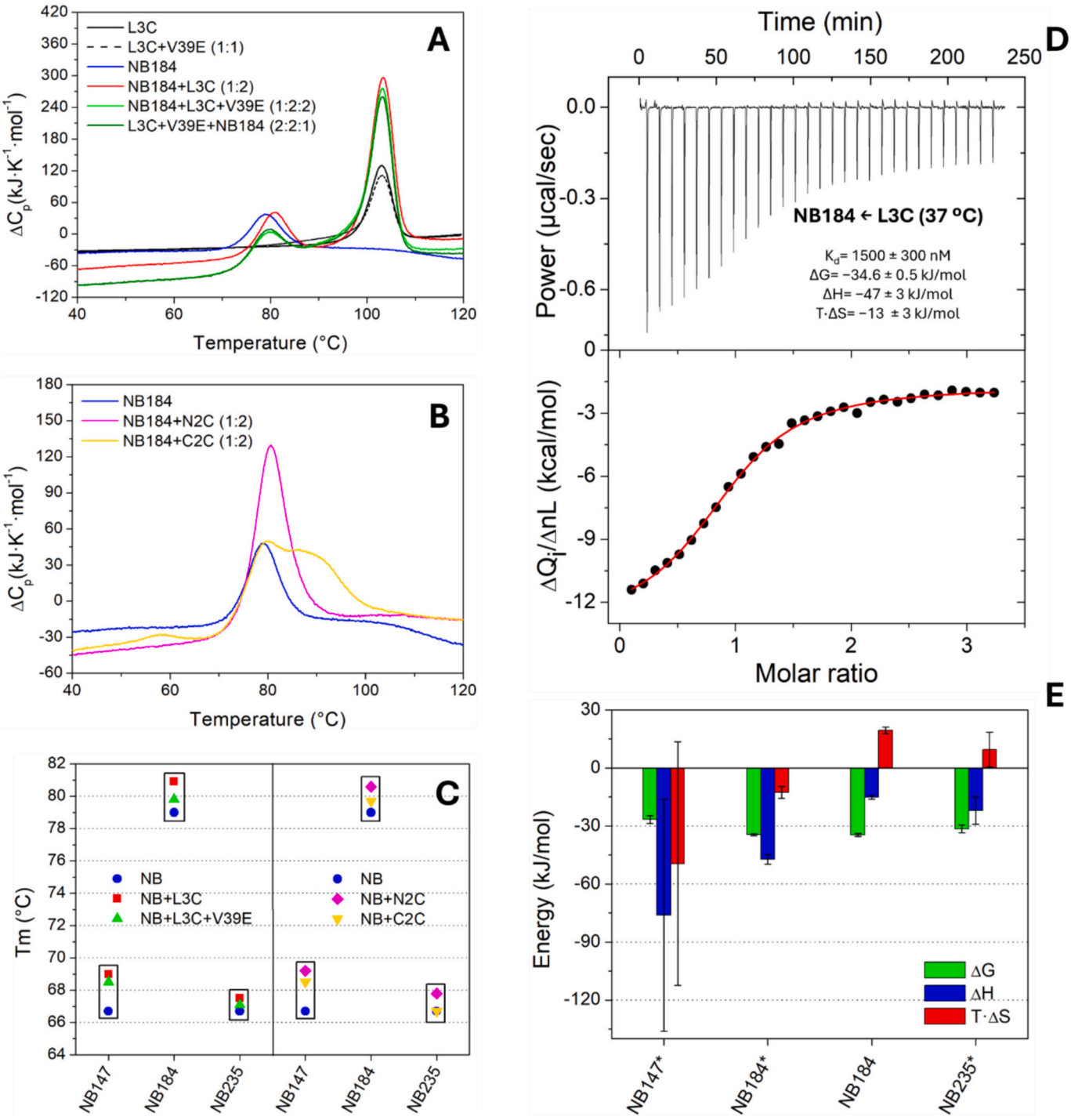

Fig. 4. DSC and ITC study of the interaction of 2nd-gen NBs with HR1. A) DSC analysis of the binding of NB184 to L3C including competition with V39E peptide. B) DSC analysis of the binding of NB184 to C2C and N2C proteins. In this case, the T_m of the NB overlaps with the T_m of N2C, but a slight increment can still be detected. C) Plot representing the effects of binding on the NB melting temperatures. Left: T_m of each NB alone, bound to L3C, and in the competition experiment with V39E peptide. Right: T_m of the N2C/C2C binding experiment. D) ITC titration of L3C with NB184 measured at 37 °C. The upper panel represents the experimental thermogram corrected from baseline. The lower panel shows the normalized heats per mole of added NB. The red line corresponds to the best fit using a model of n identical and independent sites. The binding stoichiometry is 1. E) Thermodynamic parameters of binding between the 2nd-genNBs and L3C obtained by ITC. The bars show the binding ΔG, ΔH, and T·ΔS terms. Error bars were calculated from 95 % confidence intervals of the parameters estimated by the individual fits of the binding isotherm using a model of *n* independent sites. The low affinities of NB147 and NB235 led to a parabolical shape of the binding isotherms (see Fig. S10), hence the high errors bars when obtaining the parameters ΔH and T · ΔS, which should be considered just as estimations for NB147. The asterisks (*) indicate experiments carried out at 37 °C.

the other two ($K_{d,\ 37\ °C}$ = 1.5 μM). Thermodynamic parameters, including ΔG, ΔH, T·ΔS, and stoichiometry, were derived from the experimental data (Fig. 4E, Table S5). Compared to the 1st-gen NBs, the binding enthalpy of the best of the 2nd-gen NB184 is considerably less negative, whereas the binding entropy is favorable.

3.6. SARS-CoV-2 *in vitro* neutralization assays

1st-gen NBs and 2nd-gen NBs were used in SARS-CoV-2 infection assays with Vero76 cells to assess their ability to neutralize viral infection. Initially, we tested infection with the wild-type (WT) Italian isolate (lineage B.1, carrying the D614G mutation). Among 1st-gen NBs, only NB118 and NB113 displayed significant neutralizing activity against the WT B.1 D614G genotype (Fig. 5A), although with high IC_{50} values (NB113: 270 μg/mL, 20.5 μM; NB118: 87 μg/mL, 6.7 μM) (Fig. 5C). As expected, no neutralization was found for NB107, NB117, NB248, and NB268, likely because their epitopes are not located in the HR2 binding groove, as shown by the competition assays. Intriguingly, NB278 also lacked neutralizing activity (Fig. 5D), even though this NB exhibited one of the lowest K_d (12 ± 3 nM) in the ITC experiments with

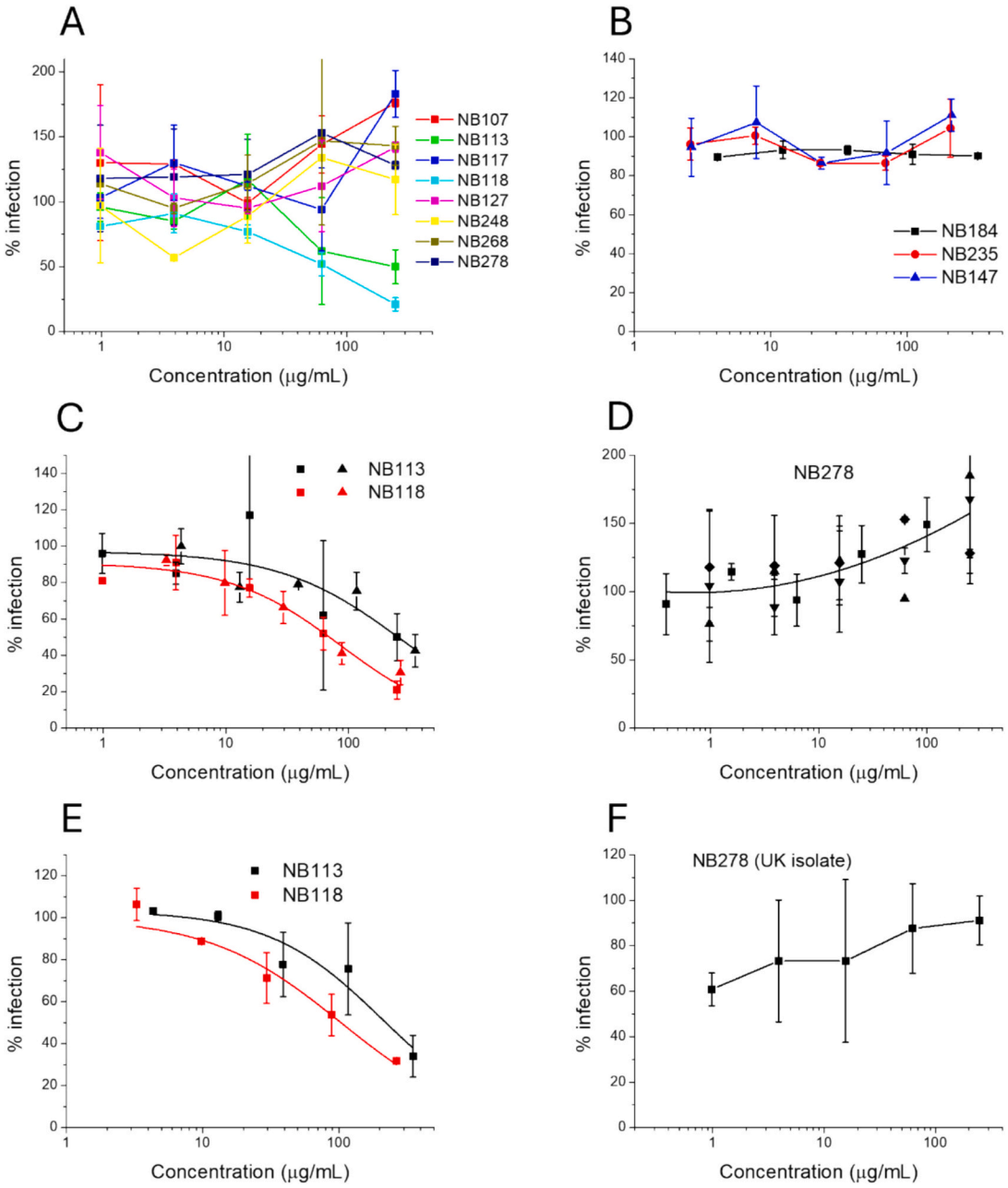

Fig. 5. SARS-CoV-2 *in vitro* neutralization assays of the 1st-gen and 2nd-gen NBs. Vero 76 cells were infected with SARS-CoV-2: WT B.1 D614G (Italian isolate) (A-D) or Alpha B.1.1.7 (UK isolate) (*E*-F), in the presence of variable concentrations of the NBs. The relative percentage of infected cells compared to the percentage of infected cells in the absence of NBs are represented in each plot as a function of NB concentration. Symbols and error bars are the average and standard deviation (S. D.) from duplicates. A) Infection with WT B1 with D614G mutation (Italian isolate) in the presence of 1st-gen NBs. B) Infection by WT B1 with D614G mutation (Italian isolate) in the presence of 2nd-gen NBs. C) Two independent experiments are indicated with different symbols for the infection with Italian isolate in the presence of NB113 or NB118. The lines correspond to the fittings using a sigmoidal Hill's function. D) Four independent experiments for the infection with Italian isolate in the presence of NB278. The polynomial line is represented for visual purposes. E) and F) Infection with B.1.1.7 (UK) isolate in the presence of NB113, NB118 (E), or NB278 (F).

L3C and competes with the HR2 peptide for binding to HR1. These findings indicate that affinity and neutralizing activity might not be totally correlated, and other factors need to be further considered. The neutralizing activity of NB113 and NB118—and the absence of such activity for NB278—was also confirmed against an Alpha B.1.1.7 UK isolate (Fig. 5E and F). None of the 2nd-gen NBs exhibited neutralizing activity (Fig. 5B). In this case, the negative outcome could likely be attributed to their low binding affinities for HR1. The K_d measured for the binding of these NBs to L3C at 37 °C ranged from 1.5 μM to 33 μM, which are up to three orders of magnitude higher than those observed at 25 °C for the best 1st-gen NBs and for the HR2-derived peptide V39E (21 ± 6 nM) [19]. Notably, only NB184 exhibited a K_d of 0.9 ± 0.3 μM (measured at 25 °C for comparative purposes) closer to the weakest candidates among the 1st-gen NBs (Fig. S10, Table S5). This reduced binding affinity of the 2nd-gen NBs, which specifically target the N-terminal half of HR1, may explain their inability to effectively compete with HR2 in the viral context and their lack of neutralizing activity in our assays.

3.7. Study of the binding cooperativity between NBs using ITC

Given that each generation of NBs targets distinct regions of HR1—specifically the C-terminal and N-terminal halves—the influence on the prebinding of one NB to L3C over the binding of a second NB was investigated using ITC (Fig. S11, Table S5). The experiments were focused on the most relevant NBs from each generation: NB113, NB118, and NB278 from the 1st generation, and NB184 from the 2nd generation. Titration at 25 °C of a preformed L3C–NB184 complex (1:2 M ratio) with any of three 1st-gen NBs resulted in a slight increase in binding affinity and Gibbs energy (Fig. 6A). However, the uncertainties in the parameters are of a magnitude similar to the observed changes. When pre-formed L3C–1st-gen NB complexes (1:1.5 M ratio) were titrated at 37 °C with NB184, more evident increments in binding Gibbs energy were observed (Fig. 6A). In these titrations, the affinity increases are primarily due to lower entropy costs, whereas the negative binding enthalpies became reduced. These findings suggest that the prior binding of a NB to either the C-terminal or N-terminal half of HR1 enhances the binding of a second NB, indicating positive binding cooperativity and allosteric communication between epitopes located in the two halves of HR1. However, this allosteric effect appears to be directional, because it is more noticeable from the C-terminal half to the N-terminal half than in the opposite direction. This observation supports the potential development of bivalent molecules capable of recognizing two distinct epitopes of HR1, provided that the targeted sites are sufficiently spaced to avoid steric constraints.

3.8. Combination neutralization assays

The cooperative binding effects observed in the ITC experiments prompted us to perform neutralization assays using combinations of 1st- and 2nd-gen NBs. Accordingly, cell infection assays were conducted with WT B.1 D614G and the Alpha B.1.1.7 UK isolate in the presence of different combinations of NB118 and NB184 (Fig. S12). No detectable synergistic effect in SARS-CoV-2 neutralization between these two NBs was observed, as the neutralizing activity of NB118 was not significantly affected by the presence of increasing concentrations of NB184. This result likely stems from the relatively low affinity of NB184, emphasizing the need for affinity optimization of this NB prior to the development potential bivalent molecules.

3.9. Epitope mapping of the HR1-targeting NBs by HDX-MS

To further delineate the location of the NB epitopes, HDX-MS was employed to investigate the binding of selected 1st- and 2nd-gen NBs to the HR1 region. Due to the high resistance of the L3C construct to pepsin digestion, a less stable variant, named L3B, was employed in these experiments, providing a peptide coverage map suitable for HDX analysis (Fig. S13). L3B and L3C differ only by a set of glycine-to-polar amino acid substitutions (mainly lysine) in L3C to increase helical propensity and prevent helix stuttering (Table S4). Importantly, as previously described [19], these mutations are orientated outside the HR2-binding crevice, ensuring that HR2 recognition remains unaffected (Fig. S14 and S15). By comparing the relative deuterium uptake in L3B alone *versus* the L3B–NB complexes, epitope mapping was achieved, revealing regions of decreased H/D exchange along the HR1 sequence due to the binding of the NB (Fig. 6B and S16-A–E). This analysis confirmed that NB113, NB118, and NB278 primarily bind to the C-terminal portion of HR1, whereas NB184 targets the N-terminal half. These four NBs induced the highest H/D exchange protection on the two parallel HR1 helices that form the HR2-binding groove, although some protection was also propagated to the opposite antiparallel helix. This is consistent with the HR2 competition observed in previous DSC and SEC experiments. In contrast, NB248 exerted the highest protection in a region located in the antiparallel HR1 helix, although some protection was propagated to the other two helices (Fig. S16—C), explaining the lack of HR2 competition found for this NB.

Notably, NB113, NB118, and NB278 also exerted protection at N-terminal end of HR1 (residues 11–15 of the first helix). This observation may explain the cooperative binding effect detected by ITC between these three NBs and NB184, suggesting that binding of one of the 1st-gen NBs to the C-terminal part of HR1 could generate a certain degree of conformational rigidification that would extend to the N-terminal part, enhancing the binding of a NB specifically targeting this region. In contrast, no significant reciprocal protection effect was detected for NB184 binding in the C-terminal region, supporting the directional character of this allosteric communication proposed from the ITC analysis. Finally, the ternary complex L3B–NB113–NB184 was studied by HDX-MS, confirming the capacity of these two NBs to simultaneously bind to HR1 with no apparent steric hindrance, reinforcing the potential of a future bivalent construct combining these two NBs.

3.10. HR1–NBs X-ray crystal structure: interactions and surface analyses

Crystallization experiments were performed using various combinations of CoVS-HR1 proteins (L3C, L3B, C2C, and N2C) and NBs (NB113, NB118, NB278, and NB184) by the vapor diffusion sitting-drop method with commercially available screening kits allowed, leading to the identification of several initial hits. However, all the crystals obtained from the different L3C–(1st-gen NBs) or L3C–(1st-gen NB–2nd-gen NB) complexes yielded poor X-ray diffraction quality due to the high solvent content of the crystals, suggesting that L3C is not suitable for crystallization. A similar limitation was found for C2C–(1st-gen NBs) complexes. Only the L3B–NB278–NB184 ternary complex produced crystals with sufficient diffraction quality for structural elucidation (Table S1).

The crystal structure of the ternary complex was solved at 2.4 Å resolution (PDB entry: 9RN6). The structure confirmed the epitope location of the two NBs (Fig. 7A) previously delineated by HDX-MS. Moreover, both NBs epitopes overlap significantly with the binding of the HR2 peptide V39E (Fig. 7B), in good consistency with the binding competition observed. Structural analysis of the ternary complex between L3B, NB278, and NB184 using the crystallographic structure was carried out to understand their differing binding affinities and thermodynamic parameters. This way, it was found that the contact surface areas at the NBs–L3B interface are quite similar, only slightly larger for NB184, and the percentages of hydrophobic surface areas buried upon binding are roughly the same (Figs. 7C–F, Table S6 and S7). Additionally, using contact-based residue-level analysis, we found that NB278 and NB184 establish a comparable number and type of intermolecular interactions with L3B (Figs. 7G–J, Table S8 and S9). According to this structural analysis, the higher affinity of NB278 compared to NB184 cannot be explained attending to significant differences in rigid-body

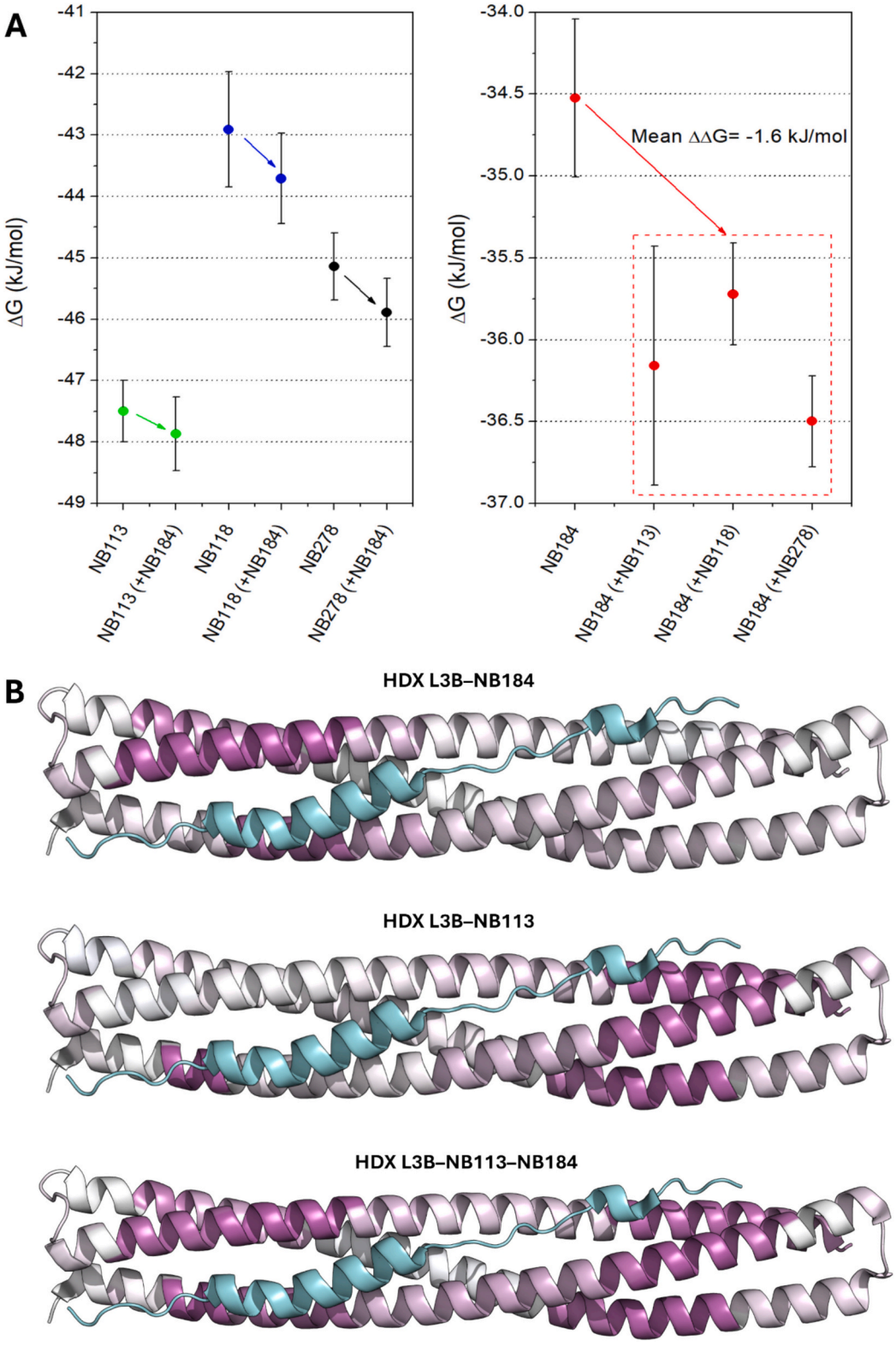

Fig. 6. A) Combined ITC binding experiments with the 1st- and 2nd-gen NBs in terms of binding ΔG. Titration with the 1st-gen NBs (NB113, NB118, and NB278) was carried out at 25 °C with a molar ratio L3C:NB184 of 1:2. Titration with NB184 was conducted at 37 °C with a molar ratio L3C:1st-gen NB of 1:1.5. B) Difference in relative deuterium uptake between a default state (L3B alone) and the protein incubated with a NB measured by HDX/MS plotted onto the crystal structure of L3B in complex with V39E peptide (PDB ID: 7ZR2). Regions colored in light purple are exchanged less within the complex with a NB while areas colored in white do not undergo any change in HDX.

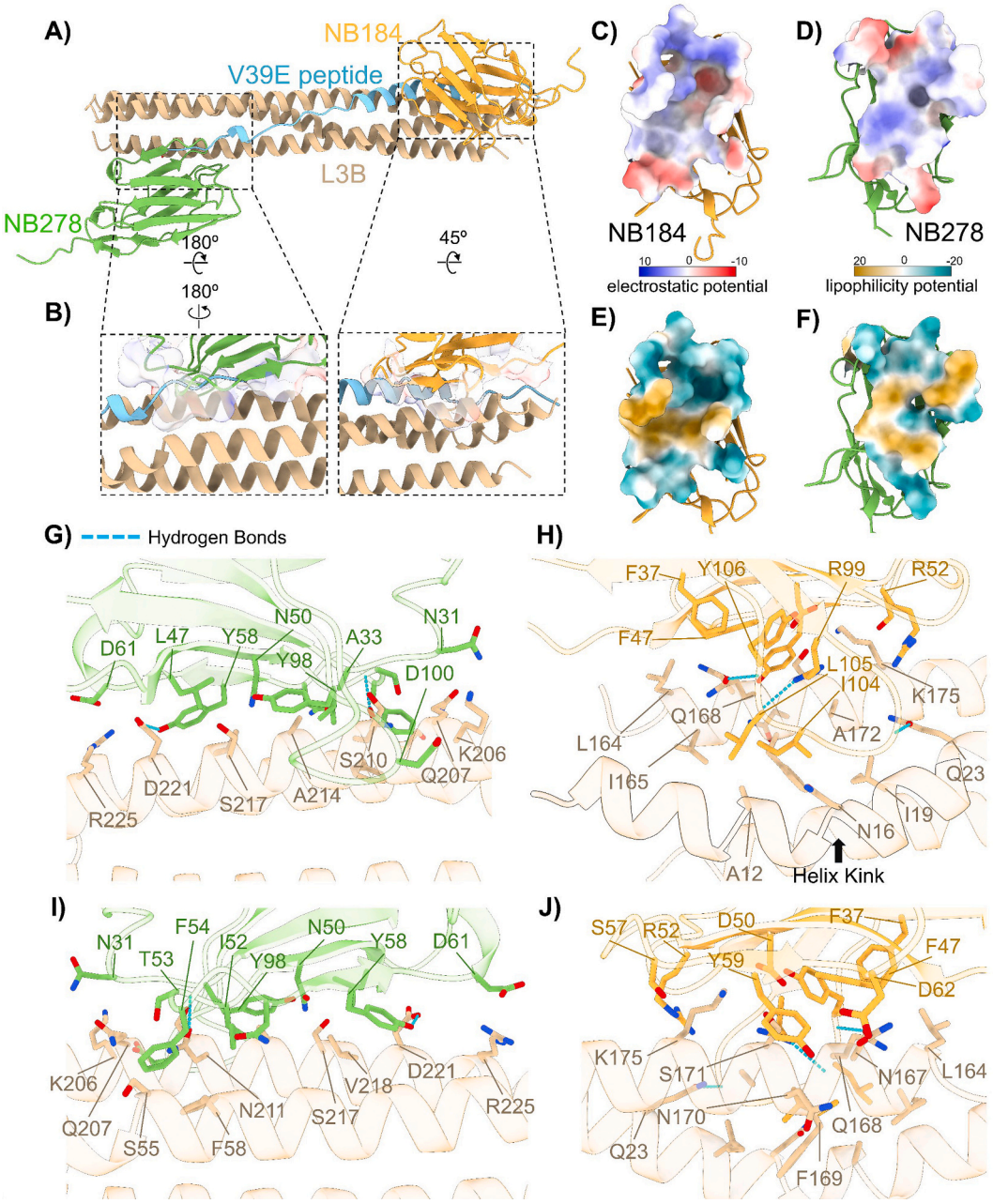

Fig. 7. Crystallographic structure of the L3B–NB184–NB278 ternary complex. A) Overall topology of the complex structure. All molecules are shown as ribbon representations and colored by molecule: L3B in khaki, NB278 in green, and NB184 in yellow. The V39E peptide (colored cyan) is included to illustrate the overlap between its binding site and those of NB278 and NB184. Atomic coordinates of V39E were taken from its complex with L3B (PDB ID: 7ZR2) and superposed onto the L3B in complex with the NBs. This second L3B molecule is omitted for the sake of clarity. B) Zoomed views of the interactions between L3B and each nanobody (NB278, left; NB184, right), highlighting the spatial overlap of V39E with the nanobody binding sites. The molecular surfaces of each NB are represented with transparency. C) and D) Contact surfaces of NB184 and NB278 respectively, colored by electrostatic potential. E) and F) contact surfaces of NB184 and NB278 colored by molecular lipophilicity potential. G) and H) Zoomed view of the contacts established between each NB and L3B displaying interacting side chains. Hydrogen bonds are shown as cyan dashed lines. In panel H), helix α1 is outlined, and the kink induced by NB184 is indicated by a black arrow. I) and J) Alternative orientations of the interactions shown in panels G) and H), respectively, rotated 180° around the y-axis to better visualize the nanobody–L3B interface.

contact surfaces and intermolecular interactions. However, it allowed the precise identification of the NBs epitopes on HR1: L_{915}–D_{935} for NB184 and V_{962}–D_{985} for NB278.

4. Discussion

Blocking HR1–HR2 interaction during SARS-CoV-2 entry has proven to be a promising strategy regarding viral inhibition. Many different strategies have been studied for this purpose, from the use of HR1/HR2 derived peptides to the far more complex neutralizing mAbs. In this work, we propose an alternative strategy based on the use of camelid derived NBs (also termed sdAbs or VHHs) targeting the highly conserved HR1 region of S2. NBs are relatively easy to select from an immune library of NBs created from the blood of an alpaca immunized with the antigen of interest. The selected NBs can be recombinantly produced in *E. coli* following simple, well-standardized purification protocols. As antigen, we have used our previously developed CoVS-HR1-L3C protein (also referred to as L3C), a faithful mimic of HR1, leading to an immune

response in the alpaca that allowed us selecting several NBs from the associated immune library. We have reported affinities in the low nM range (best $K_d = 4.7 \pm 0.9$ nM at 25 °C for NB113), mild neutralization capacity for at least two NBs, and two completely characterized epitopes within this conserved region of the Spike's S2 subunit. Overall, our results add to the growing body of evidence on the immunogenic and neutralization potential of the HR1 region in vaccine development [27,28].

Notably, the highest-affinity NBs belong to the 1st-gen NBs—those initially selected during a phage display campaign using L3C as the target. These NBs specifically recognize the C-terminal region of HR1, which may explain their low neutralization activity despite their high binding affinity. In the postfusion structure of S2, the C-terminal region of HR1 interacts with a segment of HR2 that adopts an extended conformation, whereas the N-terminal region of HR2 is predominantly arranged in a helical structure (Fig. 1B). Thus, the N-terminal region of the HR1–HR2 bundle is thought to be the core of the interaction and most HR2-derived peptides, as well as their engineered versions, mainly target the N-terminal half [12,13]. Recognizing the importance of this region, we have also isolated a second generation of NBs specifically targeting it, including at least one candidate that competes with HR2. However, none of the three 2nd-gen NBs produced have displayed measurable inhibitory activity, likely due to their very low binding affinity. Indeed, the significantly lower affinity of these 2nd-gen NBs compared to the 1st-gen explains why they have not been selected during the panning carried out with L3C as target.

The thermodynamic characterization of the NB–L3C interaction using ITC reveals clear binding enthalpy and entropy differences among NBs (Figs. 3B, 4E, Table S5). A distinct binding enthalpy reflects a different balance of interactions established between the NB and the protein (hydrogen bonds, electrostatic, van der Waals, *etc.*), as well as changes in hydration of the groups that become buried upon binding [62]. In contrast, the binding entropy is influenced by conformational changes, particularly the rigidification that occurs upon binding, as well as the desolvation of epitopes and/or paratopes on L3C and the NBs, respectively. Interestingly, NBs 113, 118, 278, and 184 possess short CDR3 compared to the other NBs (Table S2), which may contribute to their lower entropy penalties by limiting the extent of conformational rearrangement required upon binding. In addition, these NBs also compete with HR2 and target epitopes within the HR1 groove, where an entropy increase could be associated with a higher contribution of desolvation of hydrophobic surfaces, which may further mitigate the binding entropy loss.

A rigid-body analysis of the interactions observed in the crystallographic structures of the NBs–L3B ternary complex does not allow us establishing the reasons of the large affinity difference between NB184 (binding to the HR1 N-terminal half) and NB278 (binding to the C-terminal half). However, conformational changes associated with binding may play a role in explaining the observed differences in binding affinity, as well as the thermodynamic signature characteristic of each NB. As described above, binding of NB278 to the C-terminal region of HR1 exerts a significant conformational rigidification that extends to the rest of the HR1 coiled-coil, stabilizing the N-terminal half. This allosteric effect could contribute to the negative binding enthalpy of this NB, partially compensated by a negative binding entropy (Table S5). Furthermore, loops corresponding to CDR3 regions in both nanobodies were found to contribute significantly to binding, but only NB278 engages additional contacts through other CDR loops, potentially expanding its binding footprint through its own internal rigidification. In contrast, NB184 is considerably more thermostable than NB278 (Table S3) and, according to HDX-MS, its binding exerts a more localized protection on L3B. Additionally, insertion of the NB184 CDR3 into the HR1 groove produces a kink at the end of the first HR1 helix of L3B (Fig. 7H) and structural disorder on the opposing helices and the nearby loop. This may explain the lower binding enthalpy and more favorable binding entropy than NB278 at the same temperature, as measured by ITC. Collectively, these findings provide a structural rationale for the observed competition of both nanobodies with the V39E peptide and, at the same time, explain the pronounced difference in binding strength between them.

The marked affinity differences between 1st-gen and 2nd-gen NBs might also suggest the existence of a certain immunodominance effect of the C-terminal region of HR1 in its postfusion conformation, compared to the more critical N-terminal region. Certainly, it is well known that B- and T-cell immune responses are limited to a few epitopes of the potential determinants of the antigen. Immunodominance of B cells for non-neutralizing epitopes have been proved to be a major challenge during vaccine design [63]. We hypothesize that a highly immunogenic C-terminal portion of HR1 exposing epitopes with low neutralizing sensitivity could be part of an effective evasion mechanism of the virus, with key epitopes in the N-terminal region passing unnoticed to the immune system in the vulnerable stage when the pre-hairpin intermediate is extended and exposed.

It is difficult to elucidate the exact mechanism leading to this apparent immunodominance effect, as the immune response is complex in nature with many factors affecting it, such as the frequency of precursor B cells, the antigen affinity, and the antigen avidity [63]. One plausible factor could be the natural flexibility of the N-terminal region of HR1. As discussed elsewhere, the HR1 epitopes found using L3C against sera of convalescent patients are probably conformational epitopes, explaining why they had previously passed unnoticed by many epitope mapping studies using linear peptides [19]. Before B-cell presentation to helper T cell on the major histocompatibility complex (pMHC), the antigen must be processed, leading to its unfolding and proteolysis into small peptides [64]. The relationship between antigen stability and its immunogenicity is not yet well understood, with literature reporting contradictory results in this regard. However, several studies have shown that conformationally flexible proteins tend to be poorly immunogenic because their conformational epitopes are destabilized or lost due to structural fluctuations [65]. Our previous work with minimally engineered versions of the N2C and C2C proteins (CoVS-HR1 versions N and C) makes especially noticeable the intrinsic flexibility and thermal instability of the N-terminal half of the HR1 region, with a T_m of less than 25 °C at physiological pH whereas the C-terminal half mini protein exhibited a T_m of 80 °C [43]. This pronounced flexibility might be the cause of the N-terminal region rapidly losing its conformational epitopes, leading to a poorer immune response. Thus, future work should aim to improve the overall stability of N2C. In this regard, previous studies on HIV have demonstrated that by incorporating just two disulfide bonds into an HR1-mimetic mini protein (covNHR-N-dSS, analogous to the SARS-CoV-2 CoVS-HR1-N protein) the T_m can be increased by up to 40 °C [66]. Introducing disulfide bonds in a similar way should be considered a viable strategy for stabilizing the N2C protein, which could be later used as an antigen for the immunization of an alpaca and the subsequent selection of new NBs specifically targeting the core region of HR1 with increased affinity. Furthermore, NBs are very versatile molecules easily manipulable to increase their biophysical properties and affinity. Different *in vitro* and *in silico* affinity maturation approaches, or combinations of both, have been successfully applied to increased NBs affinity [67,68]. Additionally, fusion of NBs to create bivalent or bispecific constructs have proven to be an effective way to increase their overall affinity and avidity [69,70]. All these strategies combined could be implemented to improve the binding properties of NB184, which is a promising candidate capable of competing with HR2.

Very recently, during the preparation of this manuscript, Feng et al. reported the isolation of several shark-derived NBs targeting different epitopes of the S protein [70]. Among these NBs, 79C11 demonstrated the strongest binding affinity, effectively neutralized all Omicron subvariants, and prevented the infection subvariant XBB *in vivo* after nasal instillation. Using peptides covering the full length S2, 79C11 was found to recognize the epitope L_{916}–Q_{935} on HR1, which corresponds to the N-

terminal part and coincides with the epitope of NB184 reported here. However, these apparently similar NBs exhibit up to two-fold differences in binding affinity (79C11, $K_d < 35$ nM *vs* NB184, $K_d \sim 900$ nM at 25 °C). This might come with interesting considerations. First, it might be confirming that the inability of NB184 to effectively neutralize the virus could indeed stem from its lower binding affinity. Second, it might be possible that both NBs present different binding modes and subsequently different neutralization mechanisms. The authors used the native Spike (Omicron sub-variants BA.2, BA.4, and BF.7) for shark immunization, while our group employed a recombinant protein specifically mimicking the HR1 locked in its postfusion conformation. Thus, 79C11 and NB184 might be recognizing conformationally different epitopes, underlining the importance of considering this type of epitopes in future vaccine design strategies aiming at this conserved region. Future experiments studying both the ability of 79C11 to interact with CoVS-HR1-L3C and of NB184 to interact with native Spikes would help confirm this hypothesis. Overall, the work carried out by Feng et al., along with the one reported here, further reinforces the potential of NBs specifically directed against HR1 as a promising development strategy of fusion inhibitors.

Nevertheless, the lack of inhibitory capacity found here for most of the HR1-targeting NBs should not be exclusively attributed to the immunodominance phenomenon or to the low affinity of NB184 and other aspects must also be taken into consideration. SARS-CoV-2 has two distinct and mutually exclusive pathways to enter the cells, the cell surface entry and the endosomal entry. In each pathway, different host proteases participate in S protein processing, which is essential for successful membrane fusion. TMPRSS2 protease participates in the cell surface entry, which is the preferred route for the virus [6]. The cellular expression levels of this protease dictate the pathway taken by the virus. If the target cell does not express sufficient levels of TMPRSS2 protease, the virus-ACE2 complex can be internalized *via* clathrin-mediated endocytosis. Once in the endosome, cathepsin L is responsible for the S protein cleavage in a pH-dependent manner [6,71]. Vero cells used in our inhibition assays express low levels of TMPRSS2 on their surface and have been widely used as a model of endosomal entry [71–73]. Furthermore, the use of a potent inhibitor of the TMPRSS2 protease Camostat does not inhibit the virus in Vero cells, further suggesting entry in an endosome-dependent way [73]. Thus, the mild inhibitory activity observed for NB118, and to a lesser extent for NB113, could be related to endosomal viral entry. To effectively inhibit this way, the fusion inhibitors must overcome two important obstacles. First, they would need to be pre-localized with S protein in the moment of internalization, so enough concentration of inhibitor should be present in the endosome. Second, they must overcome the harsh conditions inside the late endosome such as low pH and high proteolytic activity. Acidic conditions like the ones found in the endosome throughout its different stages have been shown to hinder antigen–antibody interactions, generally reducing the Ab binding affinity [24,74]. Considering all these factors, a valuable next step to elucidate the mechanism underlying HR1–NB inhibition would be to assess their neutralization capacity in additional cell lines expressing TMPRSS2, such as Calu-3, Caco-2, or Vero cells engineered for stable TMPRSS2 expression [71].

Independently of the entry way, the epitopes' location of the NBs could be also a key determinant of their neutralizing capacity. Even though CoVS-HR1 proteins are faithful mimics of the viral HR1 and have proven to be valuable tools to study the interaction with HR2, the competition experiments performed here should not be considered a definitive answer evaluating the ability of the NBs to displace HR2. In the viral context, other factors may affect this ability, such as possible steric hindrances or kinetic effects regarding target exposure. This has been clearly exemplified by NB278, which clearly displaces HR2 in different competition assays, but fails to neutralize the virus *in vitro*.

There are potential limitations in this study related to the use of different CovS-HR1 mimics as representative of Spike's HR1. For instance, immunization was carried out with L3C, which is the most stable CovS-HR1 variant, exhibited the highest and broadest SARS-CoV-2 inhibitory activity and showed the strongest antigenicity in sera of COVID-19 patients [19]. However, the HDX-MS and crystallographic studies could only be carried out with the homologous L3B variant, which differs from L3C in several Gly-X substitutions (Figs. S14 and S15). Nevertheless, these mutations do not impact significantly on the affinity of the molecules for the HR2 peptide V39E and likely have a small effect on the NBs binding. Likewise, shortened HR1 mimics N2C and C2C, used to ascertain the regional location of the NBs epitopes and to select the 2nd-gen NBs, could have subtle conformational differences with the full HR1 groove, giving rise to less accurate epitope reproduction, weaker NB binding, or incomplete NB selection. The use of single-chain CoVS-HR1 proteins as models of the Spike's HR1 may also pose some limitations since the viral HR1 is a parallel coiled coil trimer, as opposed to the antiparallel trimer of our CovS-HR1 constructs. However, it has been demonstrated elsewhere that this strategy has many advantages in designing potent fusion inhibitors [17,19,58] and in eliciting potent anti-HIV neutralizing NBs [36].

Interestingly, we have observed that pre-binding of one NB to HR1, either to the C-terminal or the N-terminal region, appears to slightly facilitate binding of a second NB. Our group has recently studied the existing cooperativity along the HR1 crevice using the CoVS-HR1 miniproteins N and C, demonstrating that the N-terminal half of HR1 indeed harbors the core motifs of the interaction with HR2, being able to bind to peptides derived from this region and to inhibit moderately the virus. In contrast, when used on its own, the CoVS-HR1 protein mimicking the C-terminal part cannot bind HR2-derived peptides or inhibit the virus, but its presence seems to be essential for an increased affinity and overall inhibition capacity, as seen in the long CoVS-HR1 proteins containing both regions [43,44]. Cooperativity has also been described in HR2 derived peptides extended in the N-terminal region to further cover the C-terminal region of HR1 with up to 100-fold neutralization capacity compared to their 36 amino acids shorter versions [13]. This evidence seems to suggest that a good fusion inhibitor should not only be directed to the N-terminal region of HR1 but also interact with the C-terminal part. We have isolated NBs specifically targeting each of these regions which could be combined into a single biparatopic molecule that would cover the complete HR1 crevice.

Finally, it has been proven that the combination of different Abs targeting diverse epitopes on the S glycoprotein, including both S1 and S2 epitopes, can result in a stronger neutralization across different viral strains. Thus, HR1-targeting NBs could also be interesting candidates to test their capacity to aid other known neutralizing Abs and mAbs in cocktail therapy, especially useful in a constantly evolving virus such as SARS-CoV-2 [26,75].

5. Conclusions

In this work, we generated camelid-derived single-domain antibodies (Nanobodies®, NBs) against a recombinant postfusion-mimetic HR1 construct from SARS-CoV-2 (CoSV-HR1, variant L3C). Several NBs competed with HR2-derived peptides, and two candidates exhibited mild *in vitro* neutralization against two SARS-CoV-2 isolates. We identified NBs that bind specifically to each C- and N-terminal half of HR1 (1st- and 2nd-gen NBs, respectively). Notably, NBs targeting the C-terminal half of HR1 showed markedly higher affinities than those binding the N-terminal half, likely explaining the limited inhibitory capacity of the latter, and suggesting an immunodominance of the former region. Although the molecular determinants governing these affinity differences remain to be fully elucidated, they may involve conformational changes in HR1 as well as structural properties inherent to each NB. Finally, we observed cooperative binding effects between representatives of the 1st- and 2nd-gen NBs, underscoring their potential to be combined into biparatopic constructs. Overall, our findings highlight the HR1 region as a viable target for the development of next-generation fusion inhibitors and support further engineering of multivalent NB-

based therapeutics against SARS-CoV-2.

CRediT authorship contribution statement

Daniel Polo-Megías: Writing – original draft, Methodology, Investigation, Formal analysis, Data curation. **Mario Cano-Muñoz:** Writing – review & editing, Investigation, Formal analysis, Data curation. **Philipp Trolese:** Investigation, Formal analysis, Data curation. **Sara Lestani:** Investigation. **Ilaria La Rocchia:** Investigation. **Andrea Pierangelini:** Investigation, Formal analysis. **Benedetta Fongaro:** Investigation. **Patrizia Polverino de Laureto:** Writing – review & editing, Visualization, Methodology, Investigation, Formal analysis, Data curation. **Francisco J. Morales-Yánez:** Writing – review & editing, Methodology, Investigation, Formal analysis, Data curation. **Jonathan Vaneyck:** Writing – review & editing, Methodology, Investigation, Formal analysis, Data curation. **Alain Vanderplasschen:** Methodology. **Thomas Decoville:** Investigation. **Géraldine Laumond:** Investigation. **M. Carmen Salinas-Garcia:** Methodology, Investigation. **Ana Cámara-Artigas:** Writing – review & editing, Visualization, Methodology, Investigation, Formal analysis, Data curation. **José A. Gavira:** Methodology, Investigation, Formal analysis, Data curation. **Christiane Moog:** Writing – review & editing, Validation, Supervision, Project administration, Methodology, Funding acquisition, Formal analysis, Data curation. **Mireille Dumoulin:** Writing – review & editing, Validation, Supervision, Project administration, Methodology, Funding acquisition, Formal analysis, Data curation. **Francisco Conejero-Lara:** Writing – original draft, Validation, Supervision, Project administration, Methodology, Investigation, Funding acquisition, Formal analysis, Data curation, Conceptualization.

Declaration of competing interest

The authors declare that they have no known competing financial interests or personal relationships that could have appeared to influence the work reported in this paper.

Acknowledgements

This research was funded by grant PID2019.107515RB.C21 from the Spanish State Research Agency (SRA/10.13039/501100011033). Additional support was provided by ANRS (Agence Nationale de Recherches sur le SIDA et les hépatites virales), the Investissements d'Avenir program administered by the ANR (grant ANR-10-LABX-77), and EHVA (Grant No. 681032, Horizon 2020), with co-funding from the ERDF/ESF under the initiatives “A way to make Europe” and “Investing in your future.” We are also grateful to the Andalusian Regional Government for the predoctoral fellowship awarded to Daniel Polo-Megías. Mario Cano-Muñoz was supported by a Postdoctoral Research Program from the Spanish Research Agency: Juan de la Cierva (JDC2022-049681-I). Francisco Morales-Yáñez was supported by a COS-R funding from the University of Liège. Jonathan Vaneyck was supported by CIP funding. Mireille Dumoulin is a research associate from the FRS-FNRS. We are grateful to the Spanish Radiation Synchrotron Source (ALBA), Barcelona, Spain, and the European Synchrotron Radiation Facility (ESRF), Grenoble, France, for the provision of beamtime and staff assistance at XALOC (ALBA, BAG number 2023087670) and ID30B and ID23-2 (ESRF, BAG number MX2650) beamlines during diffraction data collection. We also acknowledge the Robotein® platform of the BE Instruct-ERIC Centre for providing access to the EasyPick Microlab STARlet Hamilton workstation (https://www.robotein.uliege.be/cms/c_14301428/en/robotein). Funding for open access charge: Universidad de Granada/CBUA.

Appendix A. Supplementary data

Supplementary data to this article can be found online at https://doi.org/10.1016/j.ijbiomac.2025.150022.

Data availability

Data will be made available on request.

References

[1] D.M. Altmann, R.J. Boyton, COVID-19 vaccination: the road ahead, Science 373 (2022) 1127–1132, https://doi.org/10.1126/science.abn1755.
[2] Z. Zhou, Y. Zhu, M. Chu, Role of COVID-19 vaccines in SARS-CoV-2 variants, Front. Immunol. 13 (2022), https://doi.org/10.3389/fimmu.2022.898192.
[3] A.M. Carabelli, T.P. Peacock, L.G. Thorne, W.T. Harvey, J. Hughes, T.I. de Silva, S. J. Peacock, W.S. Barclay, T.I. de Silva, G.J. Towers, D.L. Robertson, SARS-CoV-2 variant biology: immune escape, transmission and fitness, Nat. Rev. Microbiol. 21 (2023) 162–177, https://doi.org/10.1038/s41579-022-00841-7.
[4] Y. Yuan, B. Jiao, L. Qu, D. Yang, R. Liu, The development of COVID-19 treatment, Front. Immunol. 14 (2023), https://doi.org/10.3389/fimmu.2023.1125246.
[5] B. Hu, H. Guo, P. Zhou, Z.L. Shi, Characteristics of SARS-CoV-2 and COVID-19, Nat. Rev. Microbiol. 19 (2021) 141–154, https://doi.org/10.1038/s41579-020-00459-7.
[6] C.B. Jackson, M. Farzan, B. Chen, H. Choe, Mechanisms of SARS-CoV-2 entry into cells, Nat. Rev. Mol. Cell Biol. 23 (2022) 3–20, https://doi.org/10.1038/s41580-021-00418-x.
[7] Y. Cai, J. Zhang, T. Xiao, H. Peng, S.M. Sterling, R.M. Walsh, S. Rawson, S. Rits-Volloch, B. Chen, Distinct conformational states of SARS-CoV-2 spike protein, Science 369 (2020) 1586–1592, https://doi.org/10.1126/science.abd4251.
[8] S. Xia, L. Yan, W. Xu, A.S. Agrawal, A. Algaissi, C.-T.K. Tseng, Q. Wang, L. Du, W. Tan, I.A. Wilson, S. Jiang, B. Yang, L. Lu, A pan-coronavirus fusion inhibitor targeting the HR1 domain of human coronavirus spike, Sci. Adv. 5 (2019), https://doi.org/10.1126/sciadv.aav4580.
[9] M.R. Freidel, R.S. Armen, Research Progress on spike-dependent SARS-CoV-2 fusion inhibitors and small molecules targeting the S2 subunit of spike, Viruses 16 (2024), https://doi.org/10.3390/v16050712.
[10] Shibo Jiang, Kang Lin, Nathan Strick, A. Robert Neurath, 15_Jiang S_Nature-1993_HR2 derived peptides, Nature 365 (1993) 113, https://doi.org/10.1038/365113a0.
[11] L. Lu, Q. Liu, Y. Zhu, K.H. Chan, L. Qin, Y. Li, Q. Wang, J.F.W. Chan, L. Du, F. Yu, C. Ma, S. Ye, K.Y. Yuen, R. Zhang, S. Jiang, Structure-based discovery of Middle East respiratory syndrome coronavirus fusion inhibitor, Nat. Commun. 5 (2014), https://doi.org/10.1038/ncomms4067.
[12] R.D. de Vries, K.S. Schmitz, F.T. Bovier, C. Predella, J. Khao, D. Noack, B. L. Haagmans, S. Herfst, K.N. Stearns, J. Drew-Bear, S. Biswas, B. Rockx, G. McGill, N. Valerio Dorrello, S.H. Gellman, C.A. Alabi, R.L. de Swart, A. Moscona, M. Porotto, Intranasal fusion inhibitory lipopeptide prevents direct-contact SARS-CoV-2 transmission in ferrets, Science 371 (2021) 1379–1382, https://doi.org/10.1126/science.abf4896.
[13] Kailu Yang, Chuchu Wang, Alex J.B. Kreutzberger, Ravi Ojha, Suvi Kuivanen, Sergio Couoh-Cardel, Serena Muratcioglu, Timothy J. Eisen, K. Ian White, Richard G. Held, Subu Subramanian, Kendra Marcus, Richard A. Pfuetzner, Luis Esquivies, Catherine A. Doyle, John Kuriyan, Olli Vapalahti, Giuseppe Balistreri, Tom Kirchhausen, Axel T. Brunger, Nanomolar inhibition of SARS-CoV-2 infection by an unmodified peptide targeting the prehairpin intermediate of the spike protein, Proc Natl Acad Sci U S A 40 (2022) 119, https://doi.org/10.1073/pnas.2210990119.
[14] M. Lu, S.C. Blacklow, P.S. Kim, A trimeric structural domain of the HIV-1 transmembrane glycoprotein, Nat. Struct. Biol. 2 (1995) 1075–1082, https://doi.org/10.1038/nsb1295-1075.
[15] X. Chen, L. Lu, Z. Qi, H. Lu, J. Wang, X. Yu, Y. Chen, S. Jiang, Novel recombinant engineered gp41 N-terminal heptad repeat trimers and their potential as anti-HIV-1 therapeutics or microbicides, J. Biol. Chem. 285 (2010) 25506–25515, https://doi.org/10.1074/jbc.M110.101170.
[16] D.M. Eckert, P.S. Kim, Design of potent inhibitors of HIV-1 entry from the gp41 N-peptide region, Proc. Natl. Acad. Sci. USA 98 (2001) 11187–11192, https://doi.org/10.1073/pnas.201392898.
[17] S. Crespillo, A. Cámara-Artigas, S. Casares, B. Morel, E.S. Cobos, P.L. Mateo, N. Mouz, C.E. Martin, M.G. Roger, R. El Habib, B. Su, C. Moog, F. Conejero-Lara, Single-chain protein mimetics of the N-terminal heptad-repeat region of gp41 with potential as anti-HIV-1 drugs, Proc. Natl. Acad. Sci. USA 111 (2014) 18207–18212, https://doi.org/10.1073/pnas.1413592112.
[18] W. Bi, G. Chen, B. Dang, Novel engineered SARS-CoV-2 HR1 trimer exhibits improved potency and broad-Spectrum activity against SARS-CoV-2 and its variants, J. Virol. 96 (2022), https://doi.org/10.1128/jvi.00681-22.
[19] M. Cano-Muñoz, D. Polo-Megías, A. Cámara-Artigas, J.A. Gavira, M.J. López-Rodríguez, G. Laumond, S. Schmidt, J. Demiselle, S. Bahram, C. Moog, F. Conejero-Lara, Novel chimeric proteins mimicking SARS-CoV-2 spike epitopes with broad inhibitory activity, Int. J. Biol. Macromol. 222 (2022) 2467–2478, https://doi.org/10.1016/j.ijbiomac.2022.10.031.
[20] Q. Huang, X. Han, J. Yan, Structure-based neutralizing mechanisms for SARS-CoV-2 antibodies, Emerg, Microbes Infect. 11 (2022) 2412–2422, https://doi.org/10.1080/22221751.2022.2125348.
[21] Y. Chen, X. Zhao, H. Zhou, H. Zhu, S. Jiang, P. Wang, Broadly neutralizing antibodies to SARS-CoV-2 and other human coronaviruses, Nat. Rev. Immunol. 23 (2023) 189–199, https://doi.org/10.1038/s41577-022-00784-3.

[22] W.R. Strohl, Z. Ku, Z. An, S.F. Carroll, B.A. Keyt, L.M. Strohl, Passive immunotherapy against SARS-CoV-2: from plasma-based therapy to single potent antibodies in the race to stay ahead of the variants, BioDrugs 36 (2022) 231–323, https://doi.org/10.1007/s40259-022-00529-7.
[23] Z. Cui, P. Liu, N. Wang, L. Wang, K. Fan, Q. Zhu, K. Wang, R. Chen, R. Feng, Z. Jia, M. Yang, G. Xu, B. Zhu, W. Fu, T. Chu, L. Feng, Y. Wang, X. Pei, P. Yang, X.S. Xie, L. Cao, Y. Cao, X. Wang, Structural and functional characterizations of infectivity and immune evasion of SARS-CoV-2 omicron, Cell 185 (2022) 860–871, https://doi.org/10.1016/j.cell.2022.01.019.
[24] D. Pinto, M.M. Sauer, N. Czudnochowski, J. Siong Low, M. Alejandra Tortorici, M. P. Housley, J. Noack, A.C. Walls, J.E. Bowen, B. Guarino, L.E. Rosen, J. di Iulio, J. Jerak, H. Kaiser, S. Islam, S. Jaconi, N. Sprugasci, K. Culap, R. Abdelnabi, C. Foo, L. Coelmont, I. Bartha, S. Bianchi, C. Silacci-Fregni, J. Bassi, R. Marzi, E. Vetti, A. Cassotta, A. Ceschi, P. Ferrari, P.E. Cippà, O. Giannini, S. Ceruti, C. Garzoni, A. Riva, F. Benigni, E. Cameroni, L. Piccoli, M.S. Pizzuto, M. Smithey, D. Hong, A. Telenti, F.A. Lempp, J. Neyts, C. Havenar-Daughton, A. Lanzavecchia, F. Sallusto, G. Snell, H.W. Virgin, M. Beltramello, D. Corti, D. Veesler, Broad betacoronavirus neutralization by a stem helix-specific human antibody, Science 373 (2021) 1109–1116, https://doi.org/10.1126/science.abj3321.
[25] C. Dacon, C. Tucker, L. Peng, C.-C.D. Lee, T.-H. Lin, M. Yuan, Y. Cong, L. Wang, L. Purser, J.K. Williams, C.-W. Pyo, I. Kosik, Z. Hu, M. Zhao, D. Mohan, A.J. R. Cooper, M. Peterson, J. Skinner, S. Dixit, E. Kollins, L. Huzella, D. Perry, R. Byrum, S. Lembirik, D. Drawbaugh, B. Eaton, Y. Zhang, E. Sung Yang, M. Chen, K. Leung, R.S. Weinberg, A. Pegu, D.E. Geraghty, E. Davidson, I. Douagi, S. Moir, J. W. Yewdell, C. Schmaljohn, P.D. Crompton, M.R. Holbrook, D. Nemazee, J. R. Mascola, I.A. Wilson, J. Tan, Broadly neutralizing antibodies target the coronavirus fusion peptide, Science 377 (2022) 728–735, https://doi.org/10.1126/science.abq37.
[26] C.J. Li, S.C. Chang, SARS-CoV-2 spike S2-specific neutralizing antibodies, Emerg Microbes Infect 12 (2023), https://doi.org/10.1080/22221751.2023.2220582.
[27] W. Pang, Y. Lu, Y.B. Zhao, F. Shen, C.F. Fan, Q. Wang, W.Q. He, X.Y. He, Z.K. Li, T. T. Chen, C.X. Yang, Y.Z. Li, S.X. Xiao, Z.J. Zhao, X.S. Huang, R.H. Luo, L.M. Yang, M. Zhang, X.Q. Dong, M.H. Li, X.L. Feng, Q.C. Zhou, W. Qu, S. Jiang, S. Ouyang, Y. T. Zheng, A variant-proof SARS-CoV-2 vaccine targeting HR1 domain in S2 subunit of spike protein, Cell Res. 32 (2022) 1068–1085, https://doi.org/10.1038/s41422-022-00746-3.
[28] Y. Watanabe, N. Hosokawa, M. Yoshida, T. Miura, M. Kawano, Identification of closed linear epitopes in S1-RBD and S2-HR1/2 of SARS-CoV-2 spike protein able to induce neutralizing abs, Vaccines (Basel) 11 (2023), https://doi.org/10.3390/vaccines11020287.
[29] S. Muyldermans, Nanobodies: natural single-domain antibodies, Annu. Rev. Biochem. 82 (2013) 775–797, https://doi.org/10.1146/annurev-biochem-063011-092449.
[30] Y. Watanabe, J.D. Allen, D. Wrapp, J.S. Mclellan, M. Crispin, Site-specific glycan analysis of the SARS-CoV-2 spike, Science 369 (2020) 330–333, https://doi.org/10.1126/science.abb9983.
[31] M. Dumoulin, K. Conrath, A. Van Meirhaeghe, F. Meersman, K. Heremans, L.G. J. Frenken, S. Muyldermans, L. Wyns, A. Matagne, Single-domain antibody fragments with high conformational stability, Protein Sci. 11 (2002) 500–515, https://doi.org/10.1110/ps.34602.
[32] B.K. Jin, S. Odongo, M. Radwanska, S. Magez, NANOBODIES®: a review of diagnostic and therapeutic applications, Int. J. Mol. Sci. 24 (2023), https://doi.org/10.3390/ijms24065994.
[33] S. Muyldermans, Annual review of animal biosciences applications of nanobodies 59 (2025) 19, https://doi.org/10.1146/annurev-animal-021419.
[34] C. Pain, J. Dumont, M. Dumoulin, Camelid single-domain antibody fragments: uses and prospects to investigate protein misfolding and aggregation, and to treat diseases associated with these phenomena, Biochimie 111 (2015) 82–106, https://doi.org/10.1016/j.biochi.2015.01.012.
[35] J. Xu, T. Zhou, K. McKee, B. Zhang, C. Liu, A.F. Nazzari, A. Pegu, C.H. Shen, J. E. Becker, M.F. Bender, P. Chan, A. Changela, R. Chaudhary, X. Chen, T. Einav, Y. Do Kwon, B.C. Lin, M.K. Louder, J.S. Merriam, N.C. Morano, S. O'Dell, A.S. Olia, R. Rawi, R.S. Roark, T. Stephens, I.T. Teng, E. Tourtellott-Fogt, S. Wang, E.S. Yang, L. Shapiro, Y. Tsybovsky, N.A. Doria-Rose, R. Casellas, P.D. Kwong, Ultrapotent broadly neutralizing human-llama bispecific antibodies against HIV-1, advanced, Science 11 (2024), https://doi.org/10.1002/advs.202309268.
[36] L. Sun, B. Chen, X. Liu, Y. Zhu, G. Zhang, X. Liang, L. Xing, W. Xu, S. Jiang, X. Wang, Alpaca-derived nanobody targeting the hydrophobic pocket of the HIV-1 gp41 NHR broadly neutralizes HIV-1 by blocking six-helix bundle formation, Curr Res Microb Sci 7 (2024), https://doi.org/10.1016/j.crmicr.2024.100263.
[37] M. Schoof, B. Faust, R.A. Saunders, S. Sangwan, V. Rezelj, N. Hoppe, M. Boone, C. B. Billesbølle, C. Puchades, C.M. Azumaya, H.T. Kratochvil, M. Zimanyi, I. Deshpande, J. Liang, S. Dickinson, H.C. Nguyen, C.M. Chio, G.E. Merz, M. C. Thompson, D. Diwanji, K. Schaefer, A.A. Anand, N. Dobzinski, B. Shoshana Zha, C.R. Simoneau, K. Leon, K.M. White, U. Seng Chio, M. Gupta, M. Jin, F. Li, Y. Liu, K. Zhang, D. Bulkley, M. Sun, A.M. Smith, A.N. Rizo, F. Moss, A.F. Brilot, S. Pourmal, R. Trenker, T. Pospiech, S. Gupta, B. Barsi-Rhyne, V. Belyy, A. W. Barile-Hill, S. Nock, Y. Liu, P. Walter, A. Manglik, An ultrapotent synthetic nanobody neutralizes SARS-CoV-2 by stabilizing inactive Spike, Science 13 (2020) 1473–1479, https://doi.org/10.1126/science.abe3255.
[38] J. Xu, K. Xu, S. Jung, A. Conte, J. Lieberman, F. Muecksch, J.C.C. Lorenzi, S. Park, F. Schmidt, Z. Wang, Y. Huang, Y. Luo, M.S. Nair, P. Wang, J.E. Schulz, L. Tessarollo, T. Bylund, G.Y. Chuang, A.S. Olia, T. Stephens, I.T. Teng, Y. Tsybovsky, T. Zhou, V. Munster, D.D. Ho, T. Hatziioannou, P.D. Bieniasz, M. C. Nussenzweig, P.D. Kwong, R. Casellas, Nanobodies from camelid mice and llamas neutralize SARS-CoV-2 variants, Nature 595 (2021) 278–282, https://doi.org/10.1038/s41586-021-03676-z.
[39] M.A. Rossotti, H. van Faassen, A.T. Tran, J. Sheff, J.K. Sandhu, D. Duque, M. Hewitt, X. Wen, J. Bavananthasivam, S. Beitari, K. Matte, G. Laroche, P. M. Giguère, C. Gervais, M. Stuible, J. Guimond, S. Perret, G. Hussack, M. A. Langlois, Y. Durocher, J. Tanha, Arsenal of nanobodies shows broad-spectrum neutralization against SARS-CoV-2 variants of concern in vitro and in vivo in hamster models, Commun Biol 5 (2022), https://doi.org/10.1038/s42003-022-03866-z.
[40] S. Jurado, M. Cano-Muñoz, D. Polo-Megías, F. Conejero-Lara, B. Morel, Thermodynamic dissection of the interface between HIV-1 gp41 heptad repeats reveals cooperative interactions and allosteric effects, Arch. Biochem. Biophys. 688 (2020), https://doi.org/10.1016/j.abb.2020.108401.
[41] M. Cano-muñoz, S. Cesaro, B. Morel, J. Lucas, C. Moog, F. Conejero-lara, Extremely thermostabilizing core mutations in coiled-coil mimetic proteins of hiv-1 gp41 produce diverse effects on target binding but do not affect their inhibitory activity, Biomolecules 11 (2021), https://doi.org/10.3390/biom11040566.
[42] D. Polo-Megías, M. Cano-Muñoz, P. Gantner, G. Laumond, T. Decoville, J. Grezzani, I. La Rocchia, M.C. Salinas-Garcia, A. Cámara-Artigas, J.A. Gavira, F. Conejero-Lara, C. Moog, Potent HIV-1 miniprotein inhibitors targeting highly conserved gp41 epitopes, Int. J. Biol. Macromol. 310 (2025), https://doi.org/10.1016/j.ijbiomac.2025.143157.
[43] D. Polo-Megías, M. Cano-Muñoz, A.G. Berruezo, G. Laumond, C. Moog, F. Conejero-Lara, Exploring highly conserved regions of SARS-CoV-2 spike S2 subunit as targets for fusion inhibition using chimeric proteins, Int. J. Mol. Sci. 23 (2022), https://doi.org/10.3390/ijms232415511.
[44] D. Polo-Megías, M. Cano-Muñoz, A.G. Berruezo, G. Laumond, C. Moog, F. Conejero-Lara, Investigating vulnerability of the conserved SARS-CoV-2 spike's heptad repeat 2 as target for fusion inhibitors using chimeric miniproteins, Int. J. Biol. Macromol. 262 (2024), https://doi.org/10.1016/j.ijbiomac.2024.130132.
[45] E. Pardon, T. Laeremans, S. Triest, S.G.F. Rasmussen, A. Wohlkönig, A. Ruf, S. Muyldermans, W.G.J. Hol, B.K. Kobilka, J. Steyaert, A general protocol for the generation of Nanobodies for structural biology, Nat. Protoc. 9 (2014) 674–693, https://doi.org/10.1038/nprot.2014.039.
[46] C. Louis-Jeune, M.A. Andrade-Navarro, C. Perez-Iratxeta, Prediction of protein secondary structure from circular dichroism using theoretically derived spectra, Proteins: Structure, Function and Bioinformatics 80 (2012) 374–381, https://doi.org/10.1002/prot.23188.
[47] J. Juanhuix, F. Gil-Ortiz, G. Cuní, C. Colldelram, J. Nicolás, J. Lidón, E. Boter, C. Ruget, S. Ferrer, J. Benach, Developments in optics and performance at BL13-XALOC, the macromolecular crystallography beamline at the Alba synchrotron, J. Synchrotron Radiat. 21 (2014) 679–689, https://doi.org/10.1107/S160057751400825X.
[48] C. Vonrhein, C. Flensburg, P. Keller, A. Sharff, O. Smart, W. Paciorek, T. Womack, G. Bricogne, Data processing and analysis with the autoPROC toolbox, Acta Crystallogr. D Biol. Crystallogr. 67 (2011) 293–302, https://doi.org/10.1107/S0907444911007773.
[49] J. Agirre, M. Atanasova, H. Bagdonas, C.B. Ballard, A. Baslé, J. Beilsten-Edmands, R.J. Borges, D.G. Brown, J.J. Burgos-Mármol, J.M. Berrisford, P.S. Bond, I. Caballero, L. Catapano, G. Chojnowski, A.G. Cook, K.D. Cowtan, T.I. Croll, J.É. Debreczeni, N.E. Devenish, E.J. Dodson, T.R. Drevon, P. Emsley, G. Evans, P. R. Evans, M. Fando, J. Foadi, L. Fuentes-Montero, E.F. Garman, M. Gerstel, R. J. Gildea, K. Hatti, M.L. Hekkelman, P. Heuser, S.W. Hoh, M.A. Hough, H. T. Jenkins, E. Jiménez, R.P. Joosten, R.M. Keegan, N. Keep, E.B. Krissinel, P. Kolenko, O. Kovalevskiy, V.S. Lamzin, D.M. Lawson, A.A. Lebedev, A.G. W. Leslie, B. Lohkamp, F. Long, M. Malý, A.J. McCoy, S.J. McNicholas, A. Medina, C. Millán, J.W. Murray, G.N. Murshudov, R.A. Nicholls, M.E.M. Noble, R. Oeffner, N.S. Pannu, J.M. Parkhurst, N. Pearce, J. Pereira, A. Perrakis, H.R. Powell, R. J. Read, D.J. Rigden, W. Rochira, M. Sammito, F. Sánchez Rodríguez, G. M. Sheldrick, K.L. Shelley, F. Simkovic, A.J. Simpkin, P. Skubak, E. Sobolev, R. A. Steiner, K. Stevenson, I. Tews, J.M.H. Thomas, A. Thorn, J.T. Valls, V. Uski, I. Usón, A. Vagin, S. Velankar, M. Vollmar, H. Walden, D. Waterman, K.S. Wilson, M.D. Winn, G. Winter, M. Wojdyr, K. Yamashita, The CCP4 suite: integrative software for macromolecular crystallography, Acta Crystallogr D Struct Biol 79 (2023) 449–461, https://doi.org/10.1107/S2059798323003595.
[50] G. Bunkóczi, N. Echols, A.J. McCoy, R.D. Oeffner, P.D. Adams, R.J. Read, Phaser. MRage: automated molecular replacement, Acta Crystallogr. D Biol. Crystallogr. 69 (2013) 2276–2286, https://doi.org/10.1107/S0907444913022750.
[51] M. Schacherl, M. Gompert, E. Pardon, T. Lamkemeyer, J. Steyaert, U. Baumann, Crystallographic and biochemical characterization of the dimeric architecture of site-2 protease, Biochim. Biophys. Acta Biomembr. 1859 (2017) 1859–1871, https://doi.org/10.1016/j.bbamem.2017.05.006.
[52] T. Kromann-Hansen, E. Louise Lange, H. Peter Sørensen, G. Hassanzadeh-Ghassabeh, M. Huang, J.K. Jensen, S. Muyldermans, P.J. Declerck, E.A. Komives, P. A. Andreasen, Discovery of a novel conformational equilibrium in urokinase-type plasminogen activator, Sci. Rep. 7 (2017) 3385, https://doi.org/10.1038/s41598-017-03457-7.
[53] P.V. Afonine, R.W. Grosse-Kunstleve, N. Echols, J.J. Headd, N.W. Moriarty, M. Mustyakimov, T.C. Terwilliger, A. Urzhumtsev, P.H. Zwart, P.D. Adams, Towards automated crystallographic structure refinement with phenix.Refine, Acta Crystallogr. D Biol. Crystallogr. 68 (2012) 352–367, https://doi.org/10.1107/S0907444912001308.
[54] P. Emsley, K. Cowtan, Coot: model-building tools for molecular graphics, Acta Crystallogr. D Biol. Crystallogr. 60 (2004) 2126–2132, https://doi.org/10.1107/S0907444904019158.

[55] P. Emsley, B. Lohkamp, W.G. Scott, K. Cowtan, Features and development of Coot, Acta Crystallogr. D Biol. Crystallogr. 66 (2010) 486–501, https://doi.org/10.1107/S0907444910007493.
[56] V.B. Chen, W.B. Arendall, J.J. Headd, D.A. Keedy, R.M. Immormino, G.J. Kapral, L. W. Murray, J.S. Richardson, D.C. Richardson, MolProbity: all-atom structure validation for macromolecular crystallography, Acta Crystallogr. D Biol. Crystallogr. 66 (2010) 12–21, https://doi.org/10.1107/S0907444909042073.
[57] R.A. Laskowski, PDBsum: summaries and analyses of PDB structures, Nucleic Acids Res. 29 (2001) 221–222, https://doi.org/10.1093/nar/29.1.221.
[58] M. Cano-Muñoz, S. Jurado, B. Morel, F. Conejero-Lara, Conformational flexibility of the conserved hydrophobic pocket of HIV-1 gp41. Implications for the discovery of small-molecule fusion inhibitors, Int. J. Biol. Macromol. 192 (2021) 90–99, https://doi.org/10.1016/j.ijbiomac.2021.09.198.
[59] E.C. Meng, T.D. Goddard, E.F. Pettersen, G.S. Couch, Z.J. Pearson, J.H. Morris, T. E. Ferrin, U.C.S.F. ChimeraX, Tools for structure building and analysis, Protein Sci. 32 (2023), https://doi.org/10.1002/pro.4792.
[60] X. Lin, L. Guo, S. Lin, Z. Chen, F. Yang, J. Yang, L. Wang, A. Wen, Y. Duan, X. Zhang, Y. Dai, K. Yin, X. Yuan, C. Yu, B. He, Y. Cao, H. Dong, J. Li, Q. Zhao, G. Lu, An engineered 5-helix bundle derived from SARS-CoV-2 S2 pre-binds sarbecoviral spike at both serological- and endosomal-pH to inhibit virus entry, Emerg, Microbes Infect. 11 (2022) 1920–1935, https://doi.org/10.1080/22221751.2022.2095308.
[61] S. Jurado, C. Moog, M. Cano-Muñoz, S. Schmidt, G. Laumond, V. Ruocco, S. Standoli, D. Polo-Megías, F. Conejero-Lara, B. Morel, Probing vulnerability of the gp41 C-terminal heptad repeat as target for Miniprotein HIV inhibitors, J. Mol. Biol. 432 (2020) 5577–5592, https://doi.org/10.1016/j.jmb.2020.08.010.
[62] V.J. Hilser, J. Gómez, E. Freire, The enthalpy change in protein folding and binding: refinement of parameters for structure-based calculations, Proteins Struct. Funct. Genet. 26 (1996) 123–133, https://doi.org/10.1002/(SICI)1097-0134(199610)26:2<123::AID-PROT2>3.0.CO;2-H.
[63] R.K. Abbott, S. Crotty, Factors in B cell competition and immunodominance, Immunol. Rev. 296 (2020) 120–131, https://doi.org/10.1111/imr.12861.
[64] N. Pishesha, T.J. Harmand, H.L. Ploegh, A guide to antigen processing and presentation, Nat. Rev. Immunol. 22 (2022) 751–764, https://doi.org/10.1038/s41577-022-00707-2.
[65] S. Scheiblhofer, J. Laimer, Y. Machado, R. Weiss, J. Thalhamer, Influence of protein fold stability on immunogenicity and its implications for vaccine design, Expert Rev. Vaccines 16 (2017) 479–489, https://doi.org/10.1080/14760584.2017.1306441.
[66] M. Cano-Muñoz, J. Lucas, L.Y. Lin, S. Cesaro, C. Moog, F. Conejero-Lara, Conformational stabilization of Gp41-mimetic Miniproteins opens up new ways of inhibiting HIV-1 fusion, Int. J. Mol. Sci. 23 (2022), https://doi.org/10.3390/ijms23052794.
[67] X. Cheng, J. Wang, G. Kang, M. Hu, B. Yuan, Y. Zhang, H. Huang, Homology modeling-based in silico affnity maturation improves the affnity of a nanobody, Int. J. Mol. Sci. 20 (2019), https://doi.org/10.3390/ijms20174187.
[68] H. Yu, G. Mao, Z. Pei, J. Cen, W. Meng, Y. Wang, S. Zhang, S. Li, Q. Xu, M. Sun, K. Xiao, In vitro affinity maturation of Nanobodies against Mpox virus A29 protein based on computer-aided design, Molecules 28 (2023), https://doi.org/10.3390/molecules28196838.
[69] Y. Xiang, S. Nambulli, Z. Xiao, H. Liu, Z. Sang, W. Paul Duprex, D. Schneidman-Duhovny, C. Zhang, Y. Shi, Versatile and multivalent nanobodies efficiently neutralize SARS-CoV-2, Science 370 (2020) 1479–1484, https://doi.org/10.1126/science.abe4747.
[70] B. Feng, C. Li, Z. Zhang, Y. Huang, B. Liu, Z. Zhang, J. Luo, Q. Wang, L. Yin, S. Chen, P. He, X. Xiong, J. Zhao, X. Niu, Z. Chen, L. Chen, A shark-derived broadly neutralizing nanobody targeting a highly conserved epitope on the S2 domain of sarbecoviruses, J. Nanobiotechnol. 23 (2025) 110, https://doi.org/10.1186/s12951-025-03150-2.
[71] J. Koch, Z.M. Uckeley, P. Doldan, M. Stanifer, S. Boulant, P. Lozach, TMPRSS2 expression dictates the entry route used by SARS-CoV-2 to infect host cells, EMBO J. 40 (2021), https://doi.org/10.15252/embj.2021107821.
[72] K. Shirato, M. Kawase, S. Matsuyama, Middle East respiratory syndrome coronavirus infection mediated by the transmembrane serine protease TMPRSS2, J. Virol. 87 (2013) 12552–12561, https://doi.org/10.1128/jvi.01890-13.
[73] M. Hoffmann, H. Kleine-Weber, S. Schroeder, N. Krüger, T. Herrler, S. Erichsen, T. S. Schiergens, G. Herrler, N.H. Wu, A. Nitsche, M.A. Müller, C. Drosten, S. Pöhlmann, SARS-CoV-2 cell entry depends on ACE2 and TMPRSS2 and is blocked by a clinically proven protease inhibitor, Cell 181 (2020) 271–280, https://doi.org/10.1016/j.cell.2020.02.052.
[74] T. Zhou, Y. Tsybovsky, J. Gorman, M. Rapp, G. Cerutti, G.Y. Chuang, P. S. Katsamba, J.M. Sampson, A. Schön, J. Bimela, J.C. Boyington, A. Nazzari, A. S. Olia, W. Shi, M. Sastry, T. Stephens, J. Stuckey, I.T. Teng, P. Wang, S. Wang, B. Zhang, R.A. Friesner, D.D. Ho, J.R. Mascola, L. Shapiro, P.D. Kwong, Cryo-EM structures of SARS-CoV-2 spike without and with ACE2 reveal a pH-dependent switch to mediate endosomal positioning of receptor-binding domains, Cell Host Microbe 28 (2020) 867–879.e5, https://doi.org/10.1016/j.chom.2020.11.004.
[75] I. Roodink, M. van Erp, A. Li, S. Potter, S.M.J. van Duijnhoven, M. Smits, A. J. Kuipers, B. Kazemier, B. Berkeveld, E. van Geffen, B.S. de Vries, D. Rijbroek, B. Boers, S. Meurs, W. Hemrika, A. Thom, B.N. Duplantis, R.A. Romijn, J.S. Houser, J.L. Bath, Y.N. Abdiche, Broad epitope coverage of therapeutic multi-antibody combinations targeting SARS-CoV-2 boosts in vivo protection and neutralization potency to corner an immune-evading virus, Biomedicines 12 (2024), https://doi.org/10.3390/biomedicines12030642.